

# Conductivity in Open-Framework Chalcogenides Tuned via Band Engineering and Redox Chemistry

Jacob McKenzie, Khoa N. Le, Dylan J. Bardgett, Kelsey A. Collins, Thomas Ericson, Michael K. Wojnar, Julie Chouinard, Stephen Golledge, Anthony F. Cozzolino, David C. Johnson, Christopher H. Hendon,\* and Carl K. Brozek\*



Cite This: *Chem. Mater.* 2022, 34, 1905–1920



Read Online

ACCESS |



Metrics & More

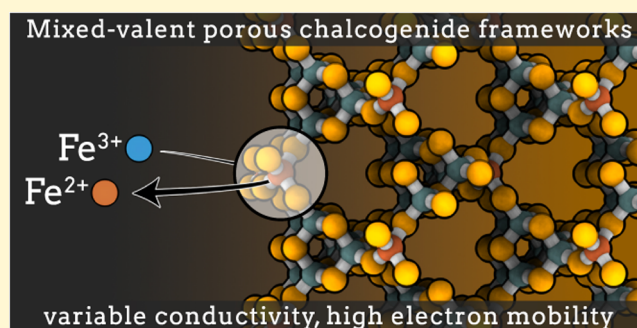


Article Recommendations



Supporting Information

**ABSTRACT:** “Open-framework chalcogenides” are an important class of materials that combine porosity with semiconductor behavior, and yet fundamental aspects of their conductivity remain unexplored. Here, we report a combined experimental–computational approach to the iconic subclass of materials  $\text{TMA}_2\text{MGe}_4\text{Q}_{10}$  (TMA = tetramethyl ammonium; M = Mn, Fe, Co, Ni, Zn; Q = S, Se). Direct current (DC) conductivity measurements and density functional theory (DFT) modeling reveal that metal ion and chalcogenide identities dominate key properties of the band structures, while impedance spectroscopy reveals purely electronic band-type transport in the Fe frameworks and redox-type mixed ion–electron conductivity in the others. Redox chemistry and computation suggest that the unique conductivity of Fe arises from its propensity toward  $\text{Fe}^{2+}/\text{Fe}^{3+}$  mixed valency as a source of p-type doping and from its highly covalent bonds that ensure high carrier mobilities. Taken together, these results demonstrate open-framework chalcogenides as a well-defined platform for understanding porous semiconductors and for achieving highly tunable electronic performance.



## INTRODUCTION

Semiconductor technologies often rely on materials with accessible porosity and high surface areas. These structural features facilitate molecular diffusion of reagents to the active sites of photo- and electrochemical catalysts<sup>1–5</sup> and improve the activity of materials such as batteries and capacitors by increasing the exposed working areas.<sup>6–11</sup> In addition to device performance, high surface-to-volume ratios present unique opportunities in interfacial chemistry. For instance, the optical, electronic, and magnetic behaviors of semiconductors can vary with the properties of the external media,<sup>12–14</sup> while high-energy surface defects can dominate the reactivity of semiconductor catalysts.<sup>15,16</sup> Studying these structure–function relationships benefits from well-defined architectures that can be tuned through precise molecular synthesis. The porosity of conventional semiconductors, such as porous metal oxides, is often irregular and difficult to modify, however.<sup>17,18</sup>

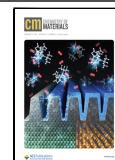
Crystalline materials with well-defined and regular porosity, such as metal–organic frameworks (MOFs), offer a powerful platform for studying the fundamental impact of high internal surface areas on wide-ranging material properties. Assembled from the combination of multitopic organic linkers and high-symmetry inorganic clusters or metal ions, MOFs have been generated into more than 90 000 structures from bottom-up synthetic routes that can be modified with molecular

specificity.<sup>19</sup> Despite this plethora of materials, few MOFs exhibit electrically conductive behavior due to the highly ionic bonding between metal ions and the typical carboxylate linkages.<sup>20</sup> Attempts to improve covalency by employing chalcogenide and azolate ligands have afforded conductive MOFs, but the examples remain compositionally limited and most extend in only two dimensions.<sup>21–23</sup> “Open-framework chalcogenides” offer an alternative family of nanoporous materials, featuring main-group-chalcogenide clusters linked by transition-metal ions through covalent bonds. Like MOFs, these materials are available with a variety of metal ions, chalcogenides, and clusters, furnishing a diverse collection of networks with varying pore sizes and shapes. Although these materials have been widely studied for decades and frequently termed semiconductors,<sup>24–37</sup> few, if any, studies have examined their basic conductivity properties.<sup>28,31,36</sup> As three-dimensional (3-D) frameworks, these materials serve as low-density analogues to conventional metal chalcogenides,

Received: December 14, 2021

Revised: January 18, 2022

Published: February 1, 2022



opening fundamental studies into the relationship of semiconductor form and function. These materials also benefit from well-defined porosity, unlike two-dimensional (2-D) metal chalcogenides whose surface areas can become inaccessible through intersheet aggregation.<sup>38,39</sup> While new examples of conductive MOFs remain hotly pursued, many open-framework chalcogenides have already been reported and simply await studies into the relationship between their nanoporosity and semiconductor behavior.

Here, we report a combined experimental–computational investigation into the iconic family of materials  $\text{TMA}_2\text{MGe}_4\text{Q}_{10}$  ( $\text{M} = \text{Mn, Fe, Co, Ni, Zn}$ ;  $\text{Q} = \text{S, Se}$ , TMA = tetramethyl ammonium), as shown in Figure 1, first reported

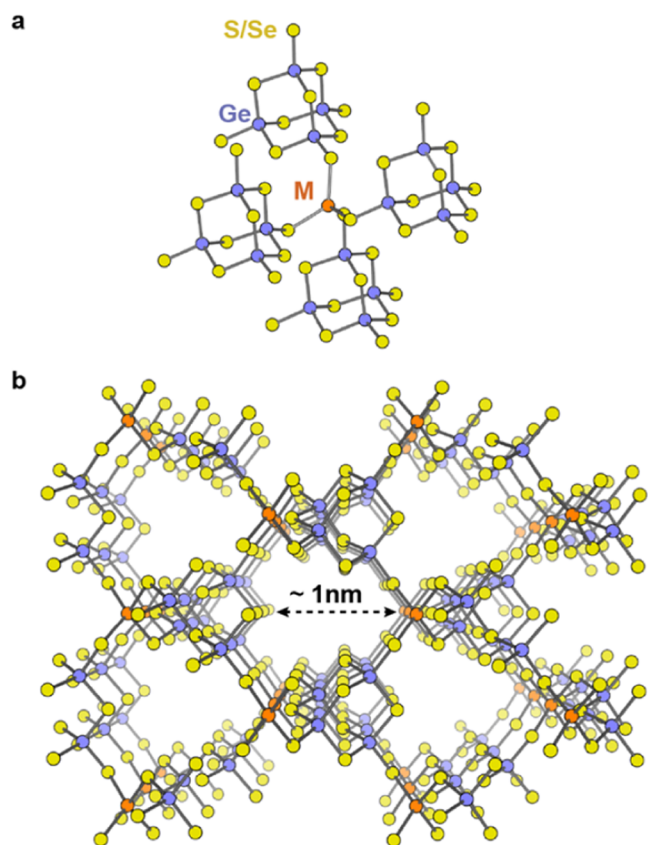


**Figure 1.** Crystal structure of open-framework chalcogenides  $\text{TMA}_2\text{MGe}_4\text{Q}_{10}$ , TMA = tetramethyl ammonium,  $\text{M} = \text{Mn, Fe, Co, Ni, Zn}$ ,  $\text{Q} = \text{S or Se}$  ( $\text{TMA}_2\text{MnGe}_4\text{S}_{10}$  depicted). (a) Local coordination and (b) extended network representations with TMA cations omitted for clarity.

by Yaghi et al. prior to the advent of modern MOF chemistry.<sup>24</sup> A reexamination of these frameworks presents new insights into their optical, magnetic, and electronic behaviors, revealing the sensitivity of these properties to subtle differences in composition and their tunability through molecular redox chemistry. The charge transport of the frameworks is especially sensitive to these variables, with conductivities differing across several orders of magnitude and in the basic mechanism of transport. A key insight from the anomalously high conductivity of the Fe analogue is that charge mobilities and charge carrier densities—the essential parameters governing conductivity—can be tuned through molecular chemistry in the form of metal–ligand bond covalency and redox chemistry. These results provide direct

confirmation of open-framework chalcogenides as porous semiconductors, while opening myriad investigations into their tunable charge transport behavior.

## RESULTS AND ANALYSIS

Following synthetic procedures previously reported by Yaghi et al.,<sup>24</sup> the open-framework chalcogenides  $\text{TMA}_2\text{MGe}_4\text{S}_{10}$  ( $\text{M} = \text{Zn}$ ;  $\text{Zn-S}$ ,  $\text{Co}$ ;  $\text{Co-S}$ ,  $\text{Fe}$ ;  $\text{Fe-S}$ , and  $\text{Mn}$ ;  $\text{Mn-S}$ ) and  $\text{TMA}_2\text{FeGe}_4\text{Se}_{10}$  ( $\text{Fe-Se}$ ) were prepared, affording crystalline powders as evidenced by powder X-ray diffraction (PXRD) (Figures S3 and S4). Le Bail fits of the PXRD patterns indexed to single-crystal diffraction data of  $\text{Mn-S}$  or  $\text{Fe-Se}$  confirmed the materials to be isostructural and phase pure. In addition to the known structures, we prepared two new isostructural members,  $\text{TMA}_2\text{NiGe}_4\text{S}_{10}$  ( $\text{Ni-S}$ ) and  $\text{TMA}_2\text{CoGe}_4\text{Se}_{10}$  ( $\text{Co-Se}$ ). Figure 2 shows the resulting experimental PXRD patterns compared to the patterns simulated from indexing, along with the fit residuals.

Table S1 summarizes the refined lattice parameters of all framework materials. The  $\text{Ni-S}$  tetragonal lattice parameters  $a$  and  $c$  index to 9.483(1) and 13.871(1) Å, respectively, indicating a unit cell contraction resulting from the reduced ionic size of  $\text{Ni}^{2+}$  as compared to that of  $\text{Mn}^{2+}$ . On the other hand, the refinement of the  $\text{Co-Se}$  cell parameters provides  $a$  and  $c$  values of 9.639(2) and 14.605(4) Å, respectively, a relative expansion of the unit cell due to the larger size of  $\text{Se}^{2-}$  as compared to that of  $\text{S}^{2-}$  in  $\text{Co-S}$  (Table S1). This expanded family of isostructural frameworks provides a platform for studying the impact of systematic changes to bonding and electronic structure on charge transport through porous materials.

To understand the relationship of the tunable compositions and the electronic properties of the  $\text{TMA}_2\text{MGe}_4\text{Q}_{10}$  frameworks, we computed the band diagrams for a variety of chalcogenides and first-row transition-metal ions in divalent and trivalent oxidation states, as summarized in Figures S20 and S21. Figure 3 plots the conduction band and valence band electron densities and corresponding density-of-state (DOS) diagrams of  $\text{Fe-S}$ ,  $\text{Ni-S}$ , and  $\text{Zn-S}$  as representative examples. Although these materials differ only in metal ions, the atomic character of the band-edge orbitals diverges considerably. For example, whereas Fe and Ni d-orbitals contribute to both band edges in  $\text{Fe-S}$  and  $\text{Ni-S}$ , respectively, S p-orbitals dominate both band edges in  $\text{Zn-S}$ . These differences are due to high-energy unpaired d electrons in  $\text{Fe-S}$  and  $\text{Ni-S}$ , which contribute substantially to the band edge(s), whereas  $\text{Zn-S}$  has no such electrons in its closed d shell. The partial atomic orbital character can be quantified for each material, as summarized in Table S3, revealing considerable differences in bond covalency, as well. For example, d-orbitals comprise 84% of the valence band in  $\text{Fe-S}$ , whereas Ni and Zn d-orbitals make up 54% in  $\text{Ni-S}$  and just 4% in  $\text{Zn-S}$ . Bond covalency also depends strongly on the metal ion oxidation state and chalcogenide identity. For example, upon oxidation, the Fe d-orbital valence band contribution drops from 84 to 72% in  $\text{Fe}^{3+}\text{-S}$  and from 71% in  $\text{Fe-S}$  to 39% in  $\text{Fe}^{3+}\text{-Se}$ . These significant differences in the electronic structures of these materials on the basis of oxidation state and chalcogenide provide a basis for understanding their diverse magnetic, optical, and charge transport behaviors.

The frameworks we expected to be paramagnetic (i.e., those containing  $\text{Mn}^{2+}$ ,  $\text{Fe}^{2+}$ ,  $\text{Co}^{2+}$ , and  $\text{Ni}^{2+}$ ) were evaluated by

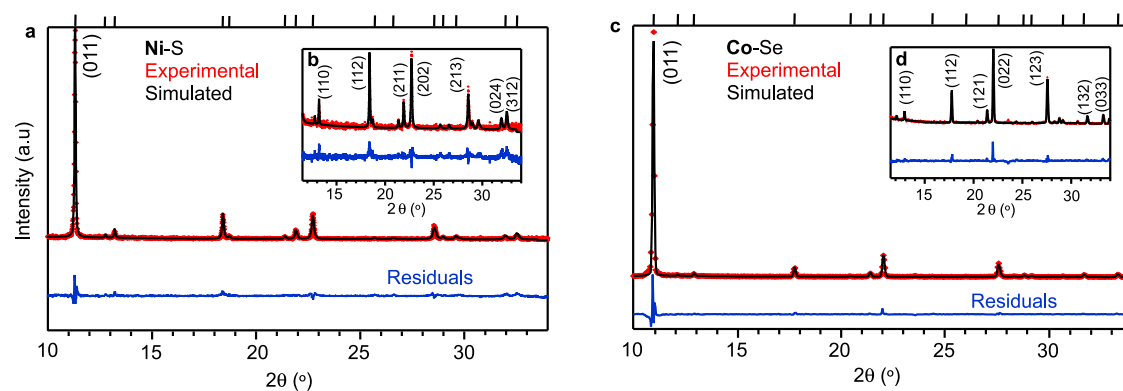


**Figure 2.** Experimental powder X-ray diffraction patterns (red) for Ni–S (a) and Co–Se (c) fitted with simulated patterns (black) and residuals (blue) after cell indexing with Le Bail fits. Insets showcase lower-intensity reflections (b, d), and tick marks on top of the plot denote expected reflections.

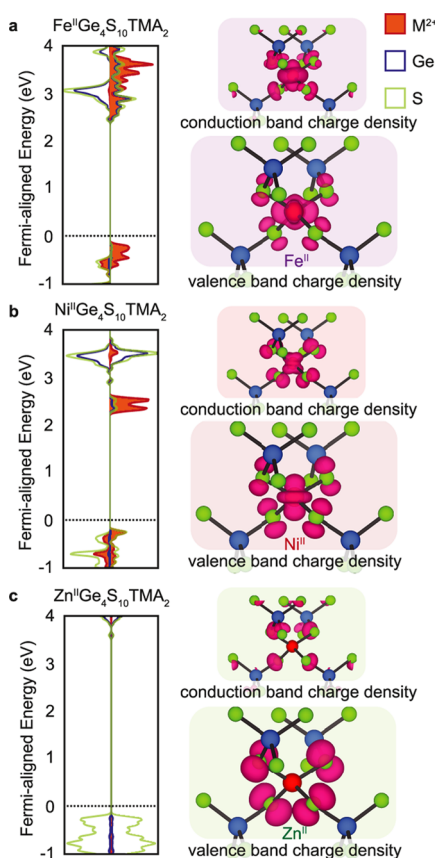


**Figure 3.** Calculated electronic structures of Fe–S (a), Ni–S (b), and Zn–S (c), with density-of-state diagrams and electron densities of valence and conduction bands, computed using the PBEsol structure, at the HSEsol06 level of theory.

SQUID magnetometry. Variable-temperature direct current (DC) magnetic susceptibility measurements of Mn–S, Co–S, and Ni–S reveal 300 K magnetic moments of 4.27, 2.32, and 1.93  $\text{cm}^3 \text{K mol}^{-1}$ . For the Mn derivative, the value of the magnetic moment is slightly below the values expected for a  $g = 2$  isolated  $\text{Mn}^{2+}$  ( $S = 5/2$ ,  $\chi_M T = 4.375 \text{ cm}^3 \text{K mol}^{-1}$ ) site. This suppression of the magnetic moment could be due to a small amount of defects at the  $\text{Mn}^{2+}$  site, resulting in slightly less than statistically one  $\text{Mn}^{2+}$  per site or radical containing S-based defects in the  $[\text{Ge}_4\text{S}_{10}]^{4-}$  cluster. For the Co derivative, the value of the magnetic moment is consistent with that

expected for a  $g = 2.2$   $\text{Co}^{2+}$  ( $S = 3/2$ ,  $\chi_M T = 2.269 \text{ cm}^3 \text{K mol}^{-1}$ ) site. For the Ni derivative, the magnetic moment is significantly higher than expected for a  $g = 2$   $\text{Ni}^{2+}$  site ( $S = 1$ ,  $\chi_M T = 1.0 \text{ cm}^3 \text{K mol}^{-1}$ ). However, a  $d^8$   $\text{Ni}^{2+}$  ion in a tetrahedral coordination environment is expected to be highly anisotropic with  $g > 2$ . For these three materials, the variable-temperature DC magnetic susceptibility measurements confirm the overall paramagnetic nature of the frameworks with negligible magnetic coupling between neighboring metal sites (Figures S9, S11, and S13). The paramagnetic nature of these materials is further reflected by their Curie–Weiss-type magnetic susceptibility and the lack of ordering as observed by alternating current (AC) magnetic susceptibility (see the Supporting Information).

Variable-temperature, DC magnetic susceptibility measurements of the Fe–S analogue reveal a more complex magnetic ground state than that observed in the previous materials. At 300 K, the magnetic moment of Fe–S is  $3.13 \text{ cm}^3 \text{K mol}^{-1}$ , consistent with an isolated high-spin  $S = 2$   $\text{Fe}^{2+}$  site. Upon cooling, the magnetic susceptibility decreases, signifying weak antiferromagnetic coupling between adjacent  $\text{Fe}^{2+}$  sites. The magnetic moment increases sharply at 3 K, consistent with either a ferromagnetic or a canted antiferromagnetic ordering event (Figure 4). To precisely determine the ordering temperature and the nature of the ordering, we collected variable-temperature AC susceptibility measurements at selected frequencies under zero applied DC field. The data

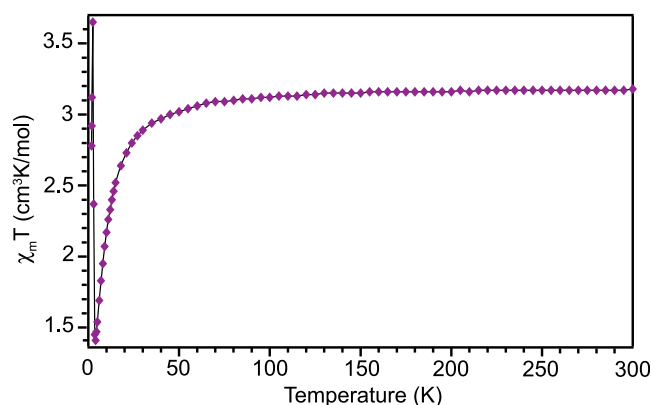


**Figure 4.** DC magnetic susceptibility for Fe–S at a 0.1 T external magnetic field strength.

show a frequency-independent peak in the in-phase ( $\chi_M'$ ) and out-of-phase ( $\chi_M''$ ) susceptibilities at 2.75 K, indicative of a magnetic ordering event. The frequency independence of the ordering suggests a true magnetic ordering event, not a spin freezing event (Figure S5). Furthermore, variable-field magnetization measurements at 1.8 K show an open hysteresis loop with a coercive field of 50 Oe (Figure S6), indicating that the Fe–S framework is a soft permanent magnet.

In contrast, the 300 K magnetic moment of Fe–Se is  $2.76 \text{ cm}^3 \text{ K mol}^{-1}$ , which is slightly less than the spin-only magnetic moment of  $3 \text{ cm}^3 \text{ K mol}^{-1}$  expected for an  $S = 2$   $\text{Fe}^{2+}$  ion and much lower than the spin-only magnetic moment of  $4.375 \text{ cm}^3 \text{ K mol}^{-1}$  expected for an  $S = 5/2$   $\text{Fe}^{3+}$  ion. To investigate the oxidation state of iron in Fe–Se, we turned to Mössbauer spectroscopy, which probes the oxidation state, coordination environment, and spin state of the iron center. At 300 K, the Mössbauer spectrum of Fe–Se (Figure 5) has a single doublet with an isomer shift of 0.393 mm/s and a quadrupole splitting of 0.568 mm/s, which we assign as high-spin  $\text{Fe}^{3+}$ , indicating the material is isovalent  $\text{Fe}^{3+}$ .<sup>40</sup>

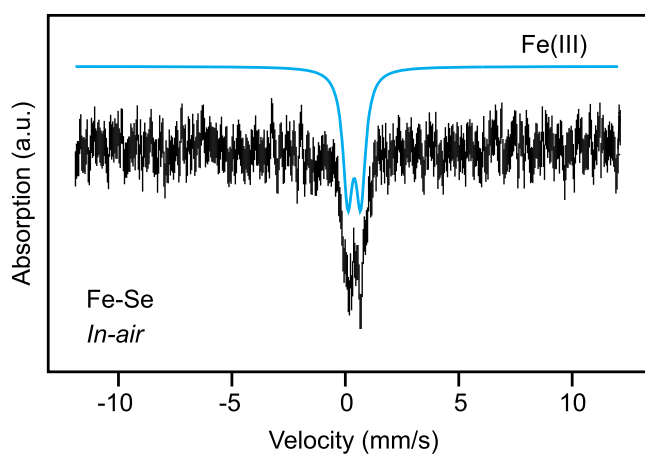


**Figure 5.** Room-temperature Mössbauer spectrum of Fe–Se prepared in-air.

As Mössbauer spectroscopy directly probes the oxidation and spin state of the iron site, the discrepancy with the DC magnetic susceptibility could be due to previously unresolved organic radicals in the  $[\text{Ge}_4\text{Se}_{10}]$  clusters. We hypothesize that the  $\text{Fe}^{2+}$  starting material used in the synthesis of the Fe–Se framework facilitates spontaneous electron transfer to the cluster, generating an  $\text{Fe}^{3+}$  site and a cluster-based radical. This *in situ* oxidation is supported by the fact that tetrahedral  $\text{Fe}^{2+}$  coordination complexes have been shown to oxidize at milder potentials when coordinated by selenium vs sulfur donors.<sup>41</sup> The  $\text{Fe}^{3+}$  spin and the radical would be strongly antiferromagnetically coupled *via* direct coupling, as reflected in the low magnetic moment of the Fe–Se framework. Below 300 K, the magnetic moment of Fe–Se continuously decreases, which is indicative of both the very strong antiferromagnetic coupling between  $\text{Fe}^{3+}$  and the  $S = 1/2$   $[\text{Ge}_4\text{Se}_{10}]$  radical and the relatively weak antiferromagnetic coupling between neighboring  $\text{Fe}^{3+}$ –radical pairs. Both the DC and AC magnetic susceptibility measurements of Fe–Se reveal no ordering event in contrast to the Fe–S system (Figures S7 and S8). We attribute this magnetic difference to the dissimilar oxidation states of iron between the two materials and the increased distance between iron centers with the expansion of the unit

cell by the larger selenide anion (Table S1). The differences in electronic configurations and subtle alterations to bonding environments in this family of materials manifest in distinct magnetic interactions ranging from long-range ordering to localized paramagnetism.

To experimentally explore the electronic structures of the framework materials, their optical absorption spectra were measured by diffuse reflectance UV–vis–NIR spectroscopy. Figure 6 plots the Kubelka–Munk transforms of Mn–S, Fe–S,

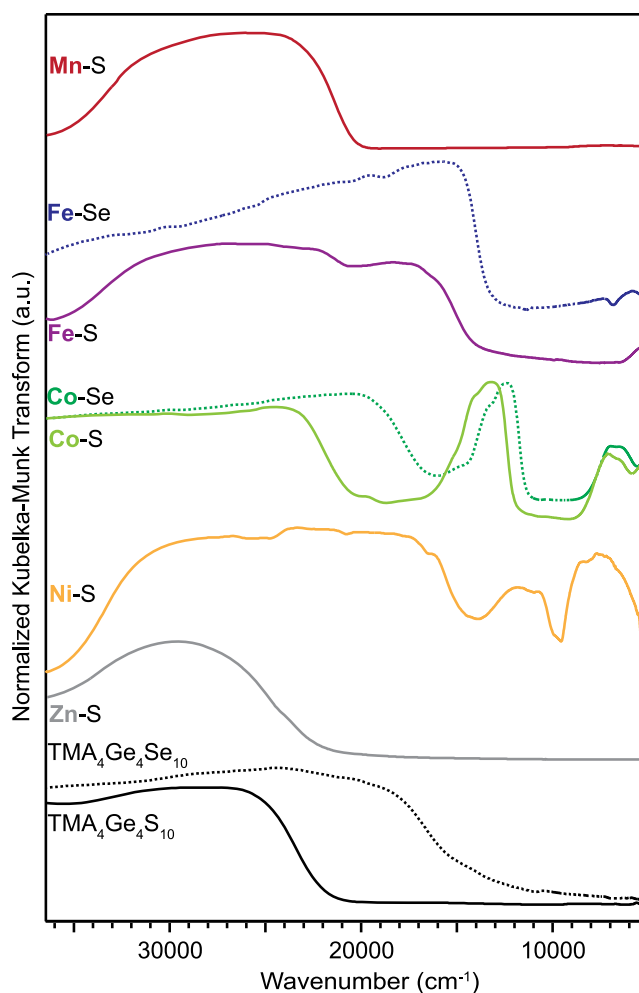


**Figure 6.** Diffuse reflectance UV–vis–NIR spectra of  $\text{TMA}_2\text{MGe}_4\text{Q}_{10}$  collected at 300 K.

Fe–Se, Co–S, Co–Se, Ni–S, Zn–S, and the parent S- and Se-based cluster compounds. In general, we assign the highest-energy absorption bands between 20 000 and 30 000  $\text{cm}^{-1}$  to the optical gap transitions and the lower-lying transitions to ligand field transitions of the  $\text{M}^{2+}$  d-orbitals subject to tetrahedrally symmetric ligand fields (Figure S15). For the frameworks lacking allowed d–d transitions (Mn–S and Zn–S), the optical gaps arise from charge-transfer events from chalcogenide p-orbital to germanium empty  $\text{sp}^3$  orbitals, with varying degrees of contributions from the metal d-orbital to the valence bands depending on the degree of metal–ligand covalency. For open-shell frameworks, the DOS diagrams in Figures 3, S20, and S21 suggest that the band-gap transitions involve a combination of S-to-Ge and ligand field transitions. The spectra in Figure 6 indicate a substantial narrowing of band-gap transitions for the open-shell systems,

which agrees with density functional theory (DFT) calculations that the conduction band involves both low-lying d-orbitals and Ge-based orbitals stabilized by approximately 1 eV relative to the wider optical gap Zn–S. Indeed, the Mn–S and Zn–S frameworks display optical gaps similar to the parent  $\text{TMA}_4\text{Ge}_4\text{S}_{10}$  cluster, whereas the open-shell frameworks exhibit narrowed gaps, suggesting that optical properties depend on the availability of d–d transitions, bond covalency, and electrostatic stabilization of atomic orbitals induced by the linking metal ions. The optical gap transitions of most materials could be assigned using Gaussian fits (Figure S17), which produced the best agreement with optical gaps determined by DFT when the band-edge orbitals were dominated by linking metal d-orbitals (Fe–S, Fe–Se, Co–S, and Ni–S) or sulfur p-orbitals (Zn–S). In contrast, Tauc plot analysis, traditionally reserved for defective and amorphous semiconductors, provided the best fits for Mn–S and Co–Se, which calculations suggest bear nearly equal contributions of chalcogenide and linking metal orbitals in the band-edge orbitals (Figure S20 and Table S2). Table 1 summarizes the

**Table 1. Optical Gap Energies ( $E_g$ ) as Determined Experimentally from Tauc and Gaussian Plots Compared against Those from Simulated Band Diagrams**

Material	Experimental $E_g$ (eV)	Simulated $E_g$ (eV)
Zn–S	3.6	3.8
Mn–S	3.4	3.2
Ni–S	2.7	2.6
Co–S	3.0	3.0
Fe–S	2.7	2.7
Fe–Se	2.0	2.2/1.9 (Fe <sup>3+</sup> )
Co–Se	2.2	2.3

experimentally derived optical gaps with values determined from simulated band structures. Together, these data demonstrate the wide tunability of the framework optical properties, with selenium increasing valence band edges relative to sulfur and  $\text{M}^{2+}$  d-orbitals dominating both band edges to produce optical gaps spanning 2.0–3.6 eV.

Ligand field analysis of the spectra in Figure 6 provides insight into how tunable compositions impact the chemical bonding and electronics of the framework materials. The high intensities of the ligand field transitions between 5000 and 15 000  $\text{cm}^{-1}$  for Fe–S, Ni–S, Co–S, and Co–Se reflect their Laporté allowed nature, as expected for tetrahedral ligand fields. Assigning these bands to the appropriate transitions and solving the corresponding Tanabe–Sugano matrices (see the Supporting Information) yields crystal field splitting energies ( $Dq$ ) spanning 392–524  $\text{cm}^{-1}$  for Fe–S, Ni–S, Co–S, and Co–Se systems (Table S2).

These comparably small  $Dq$  values are consistent with tetrahedrally symmetric chalcogenide ligand fields.<sup>42</sup> Furthermore, the smaller  $Dq$  of Co–Se (392  $\text{cm}^{-1}$ ) compared to that of Co–S (402  $\text{cm}^{-1}$ ) reflects the more diffuse nature of  $\text{Se}^{2-}$  p-orbitals. Ligand field analysis also reveals differences in the metal–ligand bond covalency in the form of the interelectronic repulsion parameter ( $B$ ). The percent reduction in  $B$  ( $B'$ ) compared to the free ion values of  $B_{\text{free ion}}$  ( $\text{Ni}^{2+} = 1080 \text{ cm}^{-1}$  and  $\text{Co}^{2+} = 1117 \text{ cm}^{-1}$ )<sup>43</sup> for each material indicates shifting of

metal-centered electron density onto ligands, i.e., covalency. We calculate  $B'$  of 46% for Co–S and 31% for Ni–S, suggesting far more covalency in the Co–S system compared to that in the Ni–S. Furthermore, the reduction is even greater for Co–Se (51%), consistent with the better matching of electronegativities between  $\text{Se}^{2-}$  and  $\text{Co}^{2+}$ , leading to greater covalency. This quantification of bond covalency complements the computational results in Table S2, showing nearly equal contributions of Co and S orbitals to the valence band in Co–S and a more polarized atomic character in Ni–S, while the valence band of Co–Se has a greater electron density contribution from Se. Differences in bond covalency and atomic character provide a basis for predicting other electronic aspects as well, such as charge transport, with greater covalency expected to engender higher charge mobilities.

Figure 7a summarizes the results of DC conductivity measurements of all frameworks using room-temperature two-electrode pressed pellet configurations. Most of the materials (Mn–S, Co–S, Co–Se, Ni–S, and Zn–S) exhibit low conductivities:  $10^{-8}$ – $10^{-9}$  S/cm, whereas Fe–S and Fe–Se displayed values typical of semiconductors:  $10^{-7}$  S/cm. To understand the origin of this large difference in conductivity, we employed electrochemical impedance spectroscopy (EIS) to probe fundamental aspects of the charge transport mechanisms. AC measurements were performed on the Fe–S and Zn–S systems because they represent the high and low conductivity extremes in this family of materials. Additionally, Fe and Zn typically exhibit markedly different redox chemistry, which we expect governs the observed conductivity. Figure 7b plots the EIS spectrum of Fe–S fitted to a parallel combination of the bulk resistance and bulk dielectric capacitance of the pellet, yielding a conductivity of 0.11  $\mu\text{S/cm}$ , which is in good agreement with the 0.23  $\mu\text{S/cm}$  found by DC measurements. Given the ion-blocking and electron transmissive nature of the two electrodes, this conductivity arises purely from electron transport.<sup>44</sup> In contrast, the Zn–S system (Figure 7c) displays a semicircle at high frequencies (low  $\text{Re}(Z)$ ) and a linear feature at low frequencies. The linear feature is modeled as a constant phase element with  $n = 0.46$  (high  $\text{Re}(Z)$ ), which is characteristic of a distorted Warburg process that we attribute to the diffusion of  $\text{TMA}^+$  ions. Fitting these data to the equivalent circuit shown in Figure 7c, often employed for mixed ion–electron conductors, produces an excellent fit, yielding a bulk conductivity far higher (0.15  $\mu\text{S/cm}$ ) than observed by DC measurements (0.024  $\mu\text{S/cm}$ ), which lack the contribution of ionic conductivity. These results imply that  $\text{TMA}^+$  ions are the dominant charge carriers in Zn–S.<sup>44</sup> The influence of ions on the charge transport mechanism of Zn–S, as well as the other low-DC conductivity materials Co–S, Mn–S, and Ni–S, is evident in DC  $I$ – $V$  curves, which appear nonlinear (non-Ohmic) (Figure S35), likely due to the simultaneous movement of both ions and charges. The  $I$ – $V$  curves eventually become linear (Ohmic) at later time points in the experiment due to the ion-blocking nature of the electrodes. DC conductivities were determined, therefore, from the linear portions of the  $I$ – $V$  curves. On the other hand, both Fe–S and Fe–Se exhibited linear (Ohmic)  $I$ – $V$  curves, suggesting that higher conductivities of the Fe systems result from a mechanism fundamentally different from the ion-coupled charge transport operative in the other frameworks.

Suspecting that the generally high redox activity of Fe contributes to the greater DC conductivities of Fe–S and Fe–Se, we investigated the effect of the Fe oxidation states on the

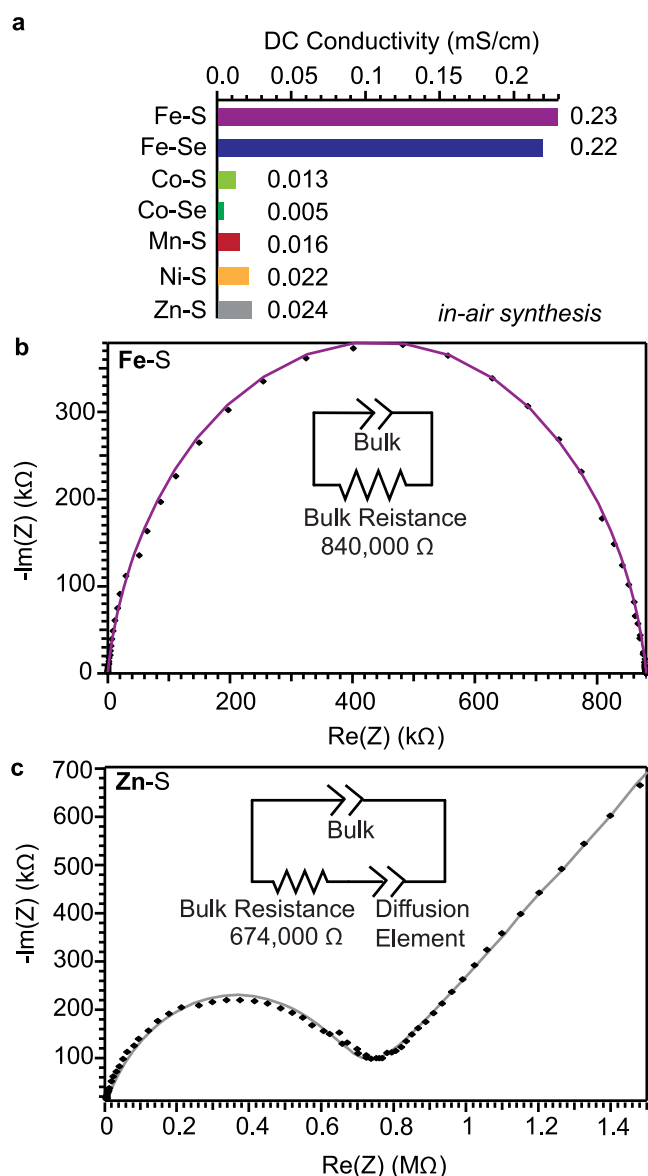


**Figure 7.** Conductivity of frameworks prepared in-air. (a) DC conductivity values of  $\text{TMA}_2\text{MGe}_4\text{Q}_{10}$  prepared in-air and measured with two-contact pressed pellet configurations at room temperature. EIS spectra of (b) Fe-S and (c) Zn-S collected at room temperature between 2 MHz and 0.1 Hz without an applied DC field and a 100 mV applied AC bias. Data are fitted to the equivalent circuits shown as insets, with fits shown as solid lines.

measured conductivity by modifying the preparation of the Fe-Q frameworks. The in-air preparation of all frameworks as reported in the data above was modified to be air-free. Specifically, whereas in-air involves preparing, isolating, washing, and drying the materials in air (see the [Methods](#) section), the synthesis, isolation, and washing steps of air-free are conducted under  $\text{N}_2$ . Furthermore, to avoid defect formation, the washing procedure was modified (see the [Methods](#) section) to allow for drying without exposure to high heat or vacuum. [Figure 8a](#) summarizes the impact of synthetic preparation on the Fe framework conductivities. When made air-free, the Fe-Q systems showed lower DC conductivities (Fe-Se gives 0.011  $\mu\text{S}/\text{cm}$  and Fe-S gives 0.13  $\mu\text{S}/\text{cm}$ ).

To further probe the Fe oxidation states resulting from these methods, room-temperature Mössbauer spectra were collected.

[Figure 8b](#) plots the spectra of Fe-S prepared in-air, showing two species with isomer shifts of  $\delta = 0.31$  ( $\text{Fe}^{3+}$ ) and 0.68 ( $\text{Fe}^{2+}$ ) mm/s with associated quadrupole splittings of  $\Delta E_Q = 0.55$  and 3.6 mm/s, respectively. The relative areas of the isomer shifts reveal mixed valency with 25%  $\text{Fe}^{3+}$ . In contrast to in-air Fe-S, the Mössbauer spectrum of the materials handled air-free ([Figure 8c](#)) shows two species with isomer shifts of 0.20 ( $\text{Fe}^{3+}$ ) and 0.68 ( $\text{Fe}^{2+}$ ) mm/s with associated quadrupole splittings of  $\Delta E_Q = 0.40$  and 3.6 mm/s, respectively. The relative areas of the isomer shifts reveal that the system is still mixed valent with 13%  $\text{Fe}^{3+}$ . Similarly, when Fe-Se was prepared air-free ([Figure 8d](#)), the Mössbauer spectrum shows two species with isomer shifts of 0.27 ( $\text{Fe}^{3+}$ ) and 0.64 ( $\text{Fe}^{2+}$ ) mm/s with associated quadrupole splittings of  $\Delta E_Q = 0.45$  and 3.6 mm/s, respectively. The relative areas of the isomer shifts indicate predominantly  $\text{Fe}^{2+}$  with 23%  $\text{Fe}^{3+}$ , whereas Fe-Se handled in-air shows only  $\text{Fe}^{3+}$ . The oxidation of these species even under air-free conditions is likely due to *in situ* oxidation of the  $\text{Fe}^{2+}$  sites by the oxidized cluster, as explained by the anomalous magnetism results for the in-air synthesis of Fe-Se. The presence of oxidized sulfur species is supported by XPS, which shows that even under air-free procedures Fe-S contains sulfate species with binding energies of  $\sim 168$  eV ([Figure S34](#)).

Diffuse reflectance UV-vis-NIR spectroscopy provided additional insight into the effect of sample preparation on redox state and electronic structure. [Figure 8e](#) shows a decrease in the optical gap for  $\text{Fe}^{2+}$ -S prepared air-free. Gaussian analysis indicates that the gap decreases from 2.7 to 2.5 eV ([Figure S18](#)). Because this transition likely involves a charge transfer from hybridized S(p)/Fe(d) to Ge(s) orbitals, the wider gap of Fe-S prepared in-air is consistent with the lowering of the Fermi level into the valence band caused by partial Fe oxidation. Similarly, Fe-Se prepared in-air shows a markedly decreased optical gap ([Figure 8f](#)), which Gaussian analysis fits to 2.2 eV from 2 eV, agreeing with the expected value from the simulated band structure for a  $\text{Fe}^{2+}$ -Se system ([Figure S19](#)). Furthermore, the low-energy weak transition at around 6000  $\text{cm}^{-1}$  for Fe-Se becomes weaker in the air-free synthesis. The decreased intensity with greater  $\text{Fe}^{2+}$  content suggests that this band arises from either the spin-forbidden high-spin  $\text{Fe}^{3+}$  ligand field transition  ${}^6A_1 \rightarrow {}^4T_1$  or from an intervalence charge transfer between  $\text{Fe}^{3+}$  and  $\text{Fe}^{2+}$  centers. Typically, the  $\text{Fe}^{3+}$  ligand field transition occurs closer to 8000  $\text{cm}^{-1}$  for tetrahedral metal sulfur systems, but the increased covalency and thus relatively small interelectronic repulsion of Fe-Se lower its energy.<sup>45</sup>

With evidence that the Fe framework conductivities depend on the oxidation state of Fe, we sought to further control Fe-S conductivity through deliberate chemical oxidation with ferrocenium tetrafluoroborate ( $\text{FcBF}_4$ ). To oxidize Fe-S, the air-free synthesis material was suspended in THF solutions of  $\text{FcBF}_4$  under a  $\text{N}_2$  atmosphere, followed by THF and hexane washes and drying. The washed and dried product had a marked color change from bright orange to brown. To quantify the extent of oxidation, room-temperature Mössbauer spectra were collected on the oxidized product. [Figure 9a,b](#) plots the spectra of the oxidized products of Fe-S after treatment with  $\text{FcBF}_4$  in 0.5 and 1.5 equiv, respectively. The sample treated with 0.5 equiv of  $\text{FcBF}_4$  shows two species with isomer shifts of 0.26 ( $\text{Fe}^{3+}$ ) and 0.68 ( $\text{Fe}^{2+}$ ) mm/s and associated quadrupole splittings of  $\Delta E_Q = 0.29$  and 3.6 mm/s, respectively. The relative areas of the isomer shifts reveal that the sample is 19%

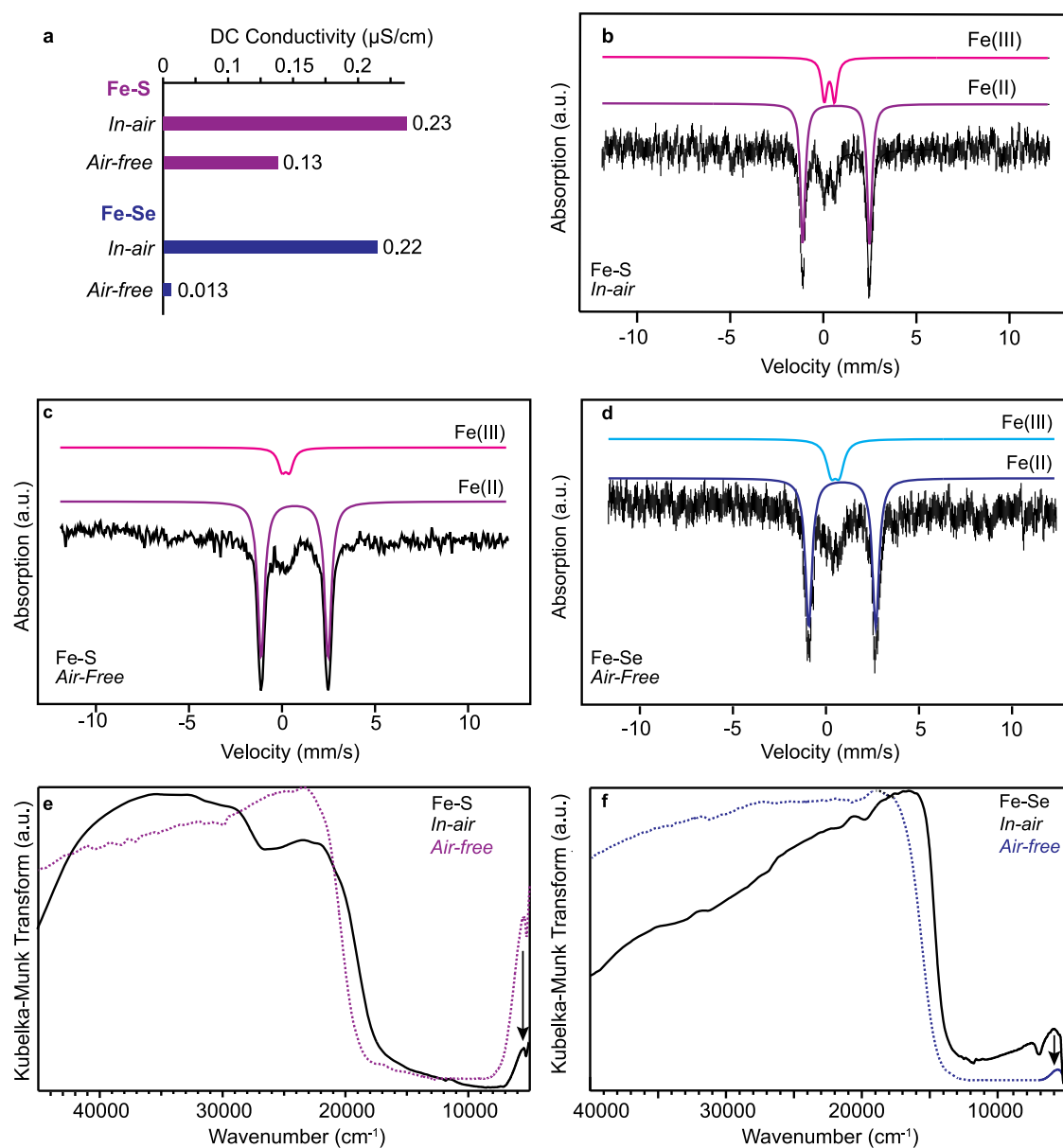


**Figure 8.** Effect of synthetic preparation on the physical properties of Fe frameworks. (a) Summary of DC conductivities, (b) Mössbauer spectrum of Fe–S prepared in-air, (c) Mössbauer spectrum of Fe–S prepared air-free, (d) Mössbauer spectrum of Fe–Se prepared air-free, (e) diffuse reflectance UV–vis–NIR spectra of Fe–S, and (f) Fe–Se frameworks.

$\text{Fe}^{3+}$ , a 6% increase from the as-synthesized air-free Fe–S material. The Fe–S treated with 1.5 equiv of  $\text{FcBF}_4$  shows two species with isomer shifts of 0.21 and 0.68 mm/s with associated quadrupole splittings of  $\Delta E_Q = 0.40$  and 3.6 mm/s, respectively. The relative areas of the isomer shifts reveal that the sample is 26%  $\text{Fe}^{3+}$ , a 13% increase from the as-synthesized air-free Fe–S material. Figure 9c compares the DC conductivity of all Fe–S samples. The results show that the DC conductivity is strongly dependent on the redox state of Fe, with higher amounts of  $\text{Fe}^{3+}$  leading to increased conductivity.

To understand how redox chemistry impacts charge transport, we collected diffuse reflectance UV–vis–NIR spectra for insight into changes to the electronic structure of the Fe–S materials, specifically the increasing or lowering of the Fermi level, i.e., redox state and number of charge carriers. Figure 9d plots the normalized spectra, with a notable

difference in the intensities of a band centered around 6000  $\text{cm}^{-1}$ . Based on assigning this feature to the spin-allowed  ${}^5E \rightarrow {}^5T_2$  d–d transition of  $T_d$   $\text{Fe}^{2+}$ , the difference in intensities corroborates air-free Fe–S containing the most  $\text{Fe}^{2+}$  centers and the oxidized 1.5 equiv  $\text{FcBF}_4$ -treated Fe–S containing the most  $\text{Fe}^{3+}$ . Furthermore, the optical gap energy shifts from 2.5 to 2.7 eV post  $\text{FcBF}_4$  treatment (Figure S26). This is the same energy shift seen when comparing the optical gap energies for air-free and in-air Fe–S syntheses. Low-energy absorption is also observed post oxidation, which is attributed to the generation of mixed-valent mid-gap states. This assignment is corroborated by the simulated band structure of  $\text{Fe}^{3+}$ –S, which showcases stabilized conduction band mid-gap states with Fe oxidation (Figure S21). PXRD confirms that materials maintain crystallinity, suggesting that these changes to conductivity and optical absorption arise from alternations to the electronics of the Fe–S framework, rather than from the

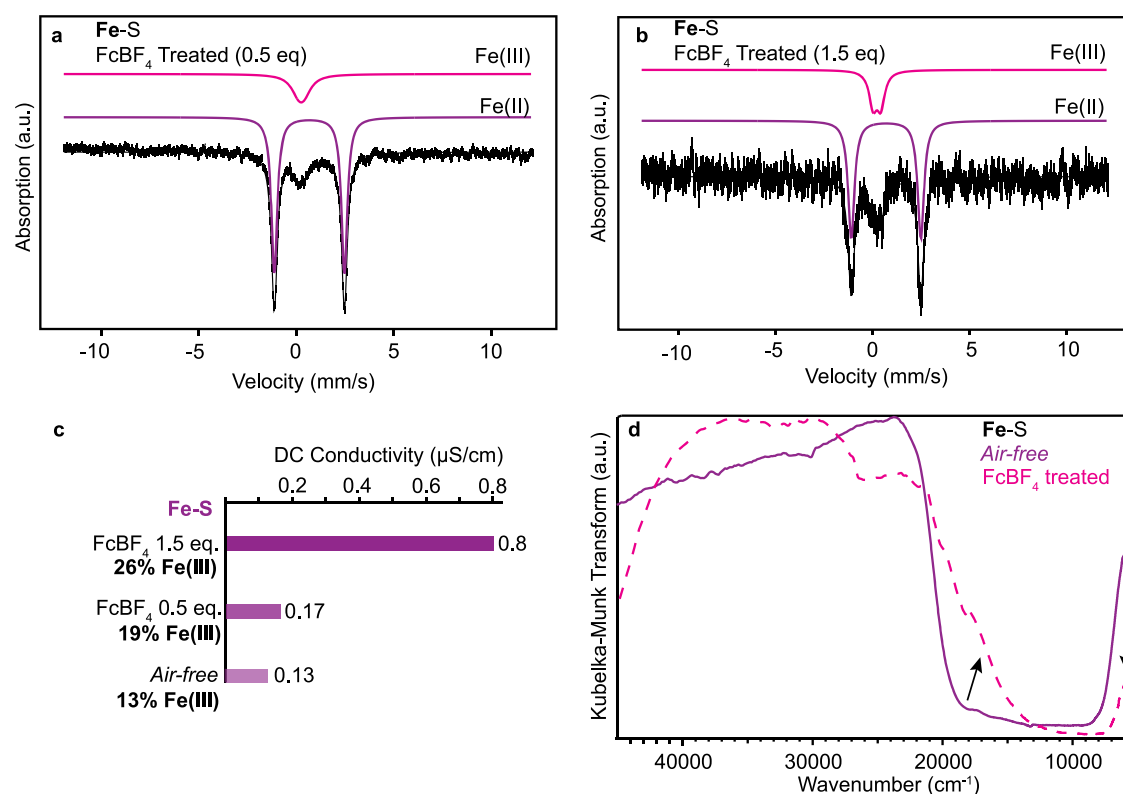


**Figure 9.** Comparison of Fe–S produced air-free *and* in-air versus postsynthetic treatment by redox reagents. (a) Room-temperature Mössbauer spectrum of Fe–S treated with 0.5 equiv of FcBF<sub>4</sub>, (b) room-temperature Mössbauer spectrum of Fe–S treated with 1.5 equiv of FcBF<sub>4</sub>, (c) summary of DC conductivity, and (d) diffuse reflectance UV–vis–NIR spectra of Fe–S in different redox states.

formation of new crystalline phases (Figure S27). To further probe the impact of Fe redox state on the charge transport in the Fe–S/Se systems, potential-dependent conductivity was performed on the Fe–S air-free system using a three-electrode setup with TBAPF<sub>6</sub> as the supporting electrolyte (more details on this experiment can be found in Methods). The EIS responses were monitored at different applied DC voltages relative to a Ag/AgNO<sub>3</sub> reference electrode, and the responses were well fitted to an equivalent circuit to extract the electronic conductivity. Figure 10 plots the electronic conductivity as a function of applied DC potential relative to the open-circuit potential (OCP). These results show that at oxidizing potentials the conductivity increases with applied potential

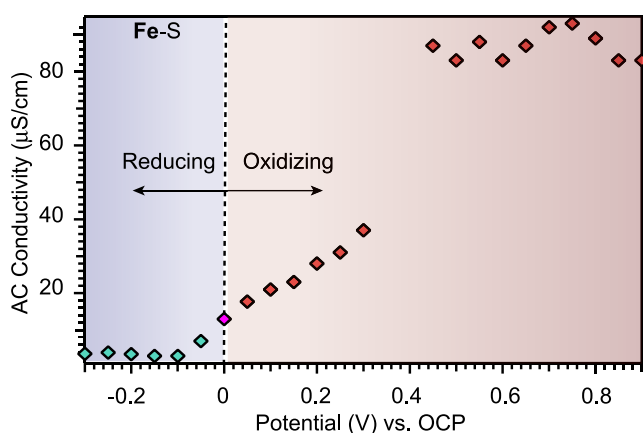


**Figure 10.** Summary of AC conductivity of air-free Fe–S as a function of applied potential with 0.1 M TBAPF<sub>6</sub> in acetonitrile.

and plateaus at higher oxidizing potentials with a large conductivity value (90 μS/cm). By contrast, the electronic conductivity is potentially independent at reducing potentials, highlighting the need for p-type carriers in the form of Fe<sup>3+</sup>.

Given the importance of Fe<sup>3+</sup> to the conductivity of the Fe frameworks, chemical oxidation was further explored to control the conductivity of the Mn, Co, and Ni materials. Figure 11a summarizes the effect of FcPF<sub>6</sub> treatment on the framework DC conductivities, indicating an increased conductivity for Mn–S but decreased for Co–S and Ni–S. Despite such significant changes to their charge transport, all frameworks retain crystallinity, as confirmed by PXRD analysis (Figure 11b). However, impurity phases forming can be detected as new unindexed peaks occurring (marked with asterisks). Unlike Co–S and Ni–S, which retained their original color, Mn–S changed from white to yellow-orange upon FcPF<sub>6</sub> treatment. Indeed, diffuse reflectance UV–vis–NIR spectra of Mn–S display a substantial shift of the absorption peak maximum upon oxidation, with Tauc analysis indicating a reduction in the optical gap energy from 3.4 to 3.3 eV (Figure S30), accompanied by increased absorption at lower energies (Figure 11c). This tailing is predicted by the simulated band structure calculations of TMAMn<sup>3+</sup>Ge<sub>4</sub>S<sub>10</sub>, which predicts stabilized conduction band mid-gap states with Mn oxidation (Figure S23). X-ray photoelectron spectroscopy (XPS) of Mn–S before and after treatment with FcPF<sub>6</sub> shows a shift toward higher binding energies for both the Mn 2p, from ~640 to ~642 eV, and S 2p, from ~161 to ~163 eV (Figure 11d,11e), suggesting the oxidation of both species that comprise the valence band. Furthermore, no Fe was detected in the XPS, confirming the absence of ferrocene or ferrocenium contamination. However, fluorine was observed in the survey



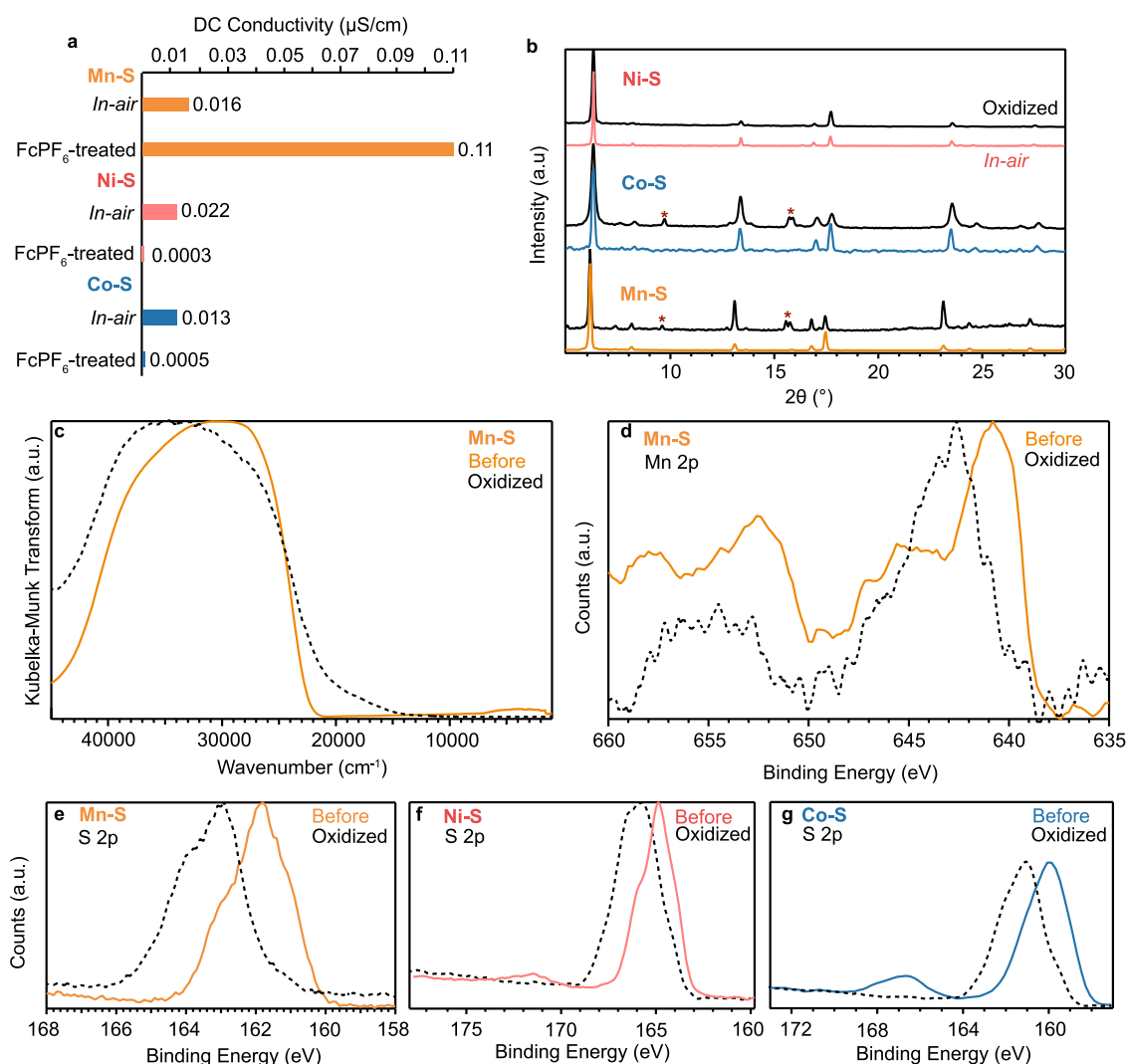


**Figure 11.** Summary of the effect of chemical oxidation on Mn-S, Co-S, and Ni-S frameworks. (a) Comparison of DC conductivities, (b) PXRD patterns, (c) Mn-S diffuse reflectance UV-vis-NIR spectra, (d) Mn 2p XPS of Mn-S, (e) S 2p XPS spectra of Mn-S, and (f) S 2p XPS spectra of Ni-S and (g) S 2p XPS spectra of Co-S before and after FcPF<sub>6</sub> treatment.

scan, indicating that some number of anions had accumulated in response to the oxidation.

In contrast, no color change was observed for Ni-S and Co-S upon treatment with FcPF<sub>6</sub>, though the FcPF<sub>6</sub> solutions changed from dark blue to orange, indicating at least partial conversion to ferrocene. The diffuse reflectance UV-vis-NIR spectra of Co-S exhibited no change in the ligand field transitions but a marked increase in the optical gap energy from 3.0 to 3.2 eV (Figure S28). Similarly, the ligand field transitions of Ni-S remained unchanged, yet, unlike Co-S, Gaussian analysis did not show any change to the optical gap energy. XPS results indicate that while Co and Ni 2p orbital binding energies do not shift after FcPF<sub>6</sub> treatment (Figures S31 and S32), the S 2p orbitals move to 164 eV (Figure 11f,11g), indicative of disulfide bond formation.<sup>46,47</sup> Taken together, these results suggest that sulfur bears the oxidation from FcPF<sub>6</sub> treatment of Co-S and Ni-S and that the frameworks are likely p-type conductors.

To confirm the charge carrier sign, the thermoelectric effect was exploited. A pressed pellet of Fe-S was heated on one end to induce a temperature gradient across the pellet and the open-circuit potential of the system was measured. The open-

circuit potential was negative, indicating that the voltage gradient ran against the temperature gradient. This behavior is indicative of a positive Seebeck coefficient, with holes as the majority charge carrier in the Fe-S system.

To understand the role of redox chemistry in the charge transport mechanism, specifically a “charge hopping” versus band-type model, we compared the band diagrams of the framework materials bearing different metal ions, chalcogenides, and redox states. Specifically, we examined the dispersions of the valence bands because holes act as the dominant charge carriers. Figure 12 summarizes the widths of the valence bands, indicating that the Fe<sup>2+</sup>-Q frameworks exhibit the greatest band dispersion. This result is expected as these bonds are the most covalent, while Zn-S shows the least covalency due to the low metal ion character. Interestingly, calculations of the Fe<sup>3+</sup>-based frameworks show lower bandwidths compared to those of the Fe<sup>2+</sup> analogues. Inspection of the geometry-optimized structures reveals a contraction of the unit cell upon oxidation to form Fe<sup>3+</sup> (Figure S22). Calculations also predict that this physical distortion causes a change in the optical gap, which helps explain the agreement between Fe and Se prepared in-air with

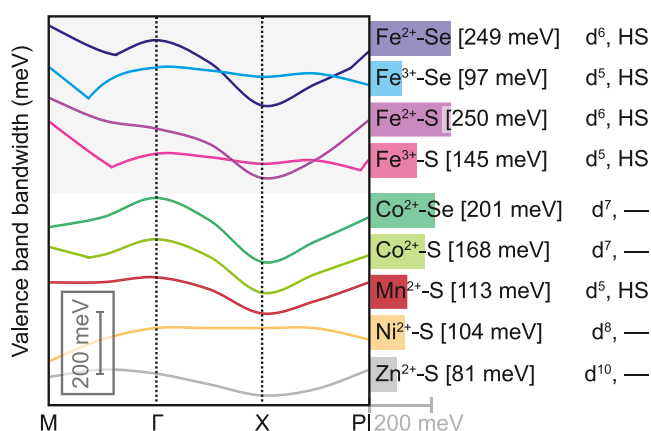


**Figure 12.** Comparison of valence band dispersions of frameworks with different metal ions, chalcogenides, and oxidation states. Diagrams of valence bands with arbitrary energy offsets for clarity. Frameworks with divalent and trivalent metal ions were simulated with two and one TMA<sup>+</sup> cations, respectively.

an optical gap of 2.0 eV compared with the simulated band structure of Fe<sup>3+</sup>-Se (1.9 eV). These results also imply that the superior conductivity of Fe frameworks, specifically those containing Fe<sup>2+</sup>, arises from the greater mobility of holes in the dispersive valence bands.

For evidence that mid-gap orbitals and Fe redox chemistry affect the different energetics of charge transport between the Fe frameworks, we measured the variable-temperature DC conductivity of Fe-S prepared under air-free and in-air synthetic conditions and Fe-Se prepared under air-free conditions. Figure 13 shows the Arrhenius plots of these materials. The in-air synthesis of Fe-S boasts the lowest activation energy (0.36 eV) and result in the highest conductivity seen of materials explored by temperature dependence. Interestingly, while having substantially different conductivities the air-free syntheses of Fe-Se and Fe-S have nearly identical activation energies, within error of each other (0.53 and 0.56 eV, respectively). These results suggest that the presence of Fe<sup>3+</sup> lowers the activation barrier by introducing charge carriers while decreasing charge mobility as a result of less dispersive bands. This effect is most pronounced for the Fe-Se system, which shows a larger decrease in conductivity compared to that for Fe-S while having a similar activation energy. Furthermore, this Arrhenius analysis explains why the in-air synthesis of Fe-Se conductivity is lower than in-air synthesis of Fe-S while being entirely Fe<sup>3+</sup> and having a far larger charge carrier density.

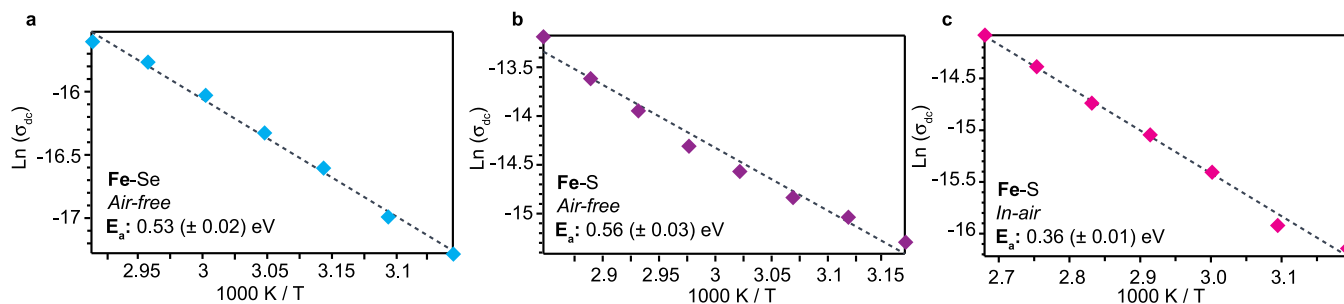
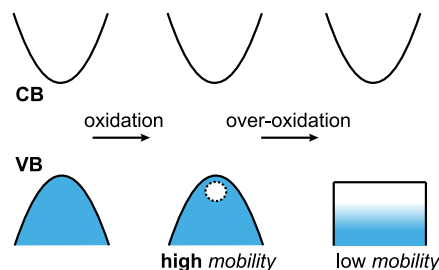


**Figure 13.** Arrhenius plots of variable DC conductivity of (a) Fe-Se prepared air-free and Fe-S prepared air-free (b) and in-air (c).

## DISCUSSION

These results suggest a band-type charge transport mechanism for the Fe-containing frameworks and a redox-hopping-type mechanism for the Mn, Co, Ni, and Zn materials. Generally, band-type transport leads to higher conductivities in materials with greater bond covalency and, hence, high charge mobilities, while redox hopping depends on chemical factors that promote outer-sphere electron transfer, as outlined by Marcus theory.<sup>48</sup> Specifically, redox hopping benefits from materials with redox sites in close proximity by improving the likelihood of charge transfer and with mixed valency to provide both donor charges and acceptor orbitals.<sup>49</sup> Our measurements indicate that holes act as the dominant charge carriers, implying that the curvatures of valence bands should dictate charge mobilities, while our calculations predict that Fe<sup>2+</sup> frameworks possess greater valence bandwidths. The EIS data in Figure 7 corroborate this assignment by showing that Fe-S charge transport involves pure electronic movement, whereas Zn-S conductivity involves the transfer of both electrons and ions, as expected for outer-sphere electron transfer to be accompanied by charge-balancing ions. While band dispersions for pristine Fe<sup>2+</sup>-Se and Fe<sup>2+</sup>-S are comparable, the dispersion drop is far more significant for Fe<sup>3+</sup>-Se than for Fe<sup>3+</sup>-S, with bands comparable to the flat valence band of Zn-S. Scheme 1

### Scheme 1. Band Diagrams Summarizing the Impact of Redox Chemistry and Framework Composition on Band Curvature, Carrier Concentrations, and Mid-Gap States



summarizes the key insight from these studies, namely, that high conductivity in these frameworks requires both higher charge carrier densities and dispersive band curvatures (high carrier mobility) but that a critical amount of oxidation causes the frameworks to distort into materials with lower charge mobilities.

The redox-dependent conductivity supports the assignment of a band-type mechanism for the Fe frameworks, as well, and explains the superior conductivity of the Fe frameworks. If the mechanism involved redox hopping, then conductivity would

maximize with  $\text{Fe}^{2+}/\text{Fe}^{3+}$  in a 50:50 mixture, with conductivity decreasing beyond this mixture, as has been observed for redox polymers.<sup>50,51</sup> Instead, the DC conductivity of Fe–S from potential-dependent conductivity (Figure 10) does not peak but rather continues to increase with greater oxidizing potentials before leveling off. Furthermore, the observation that the in-air synthesis of  $\text{Fe}^{3+}$ –Se produces a far more conductive material than the mixed-valent air-free synthesis of Fe–Se disputes a redox-hopping mechanism. For band-type materials, conductivity generally improves in materials with greater charge carrier concentrations. However, “overoxidation” of the Fe–S and Fe–Se frameworks to form the  $\text{Fe}^{3+}$  variants causes significant distortions to the lattices that flatten the valence bands and reduce hole mobility (Scheme 1). The general tendency of  $\text{Fe}^{2+}$  to engage in facile redox chemistry, therefore, implies that the higher conductivity of the Fe frameworks arises from their ability to form dilute charge carrier concentrations. Accordingly, the partial oxidation of Mn–S led to greater DC conductivity by forming an oxidized Mn species. If oxidation had led to dilute concentrations of  $\text{Ni}^{3+}$  and  $\text{Co}^{3+}$ , rather than oxidized sulfides, we predict that Ni–S and Co–S also would have demonstrated improved conductivity. Instead, we propose that the Mn, Co, and Ni frameworks show similar charge transport to Zn–S when prepared in air despite their more dispersive valence bands because, like Zn–S, their charge transport involves intra- and intercluster hopping, rather than through bonds. Similarly, among MOF families that can be prepared with a variety of metal ions, the Fe derivatives often exhibit conductivities several orders of magnitude higher and smaller activation energies. Further investigations suggest that Fe promotes charge transport with its high-energy Fe d-orbitals susceptible to oxidation and, hence,  $\text{Fe}^{2+}/^{3+}$  mixed valency,<sup>52</sup> akin to the Fe frameworks studied here.

The conductivity of the Fe–S and Fe–Se frameworks represents rare examples of the three-dimensional band-type transport in porous frameworks. High conductivity in MOFs often arises from charge delocalization along infinite one-dimensional (1-D) chains of inorganic ligands, such as chalcogenides,<sup>53–55</sup> and metal ions within otherwise 3-D frameworks. In this “through-bond” transport mechanism, orbitals are conjugated along the chains but not across the organic cores of the linkers. In rare cases, the chains are 2-D or 3-D,<sup>23,56</sup> but orbital overlap does not involve the entire material in an “extended conjugation” fashion. Extended conjugation has been observed in MOFs that employ “redox noninnocent”<sup>57</sup> or “fully conjugated” linkers,<sup>21,58–60</sup> although the examples with the highest conductivities are typically 2-D sheets. For frameworks based on polyoxometalate clusters,<sup>61</sup> the exceptional conductivity of the Fe variants likely arises from redox-type hopping, rather than from band-type transport, due to the ionic nature of  $\text{Fe}^{2+}$ – $\text{O}^{2-}$  bonds. The computed electron density in Figures 3 and S21 and Table S3 shows that the valence bands of most of the frameworks involve the metal d-orbitals and chalcogenide p-orbitals but not the Ge atoms, whereas the conduction bands involve all elements. Hole transport, therefore, does not proceed strictly by “extended conjugation”, whereas n-type doping would lead to such a mechanism. Although open-framework chalcogenides comprise a large and important family of materials, few reports have investigated their charge transport properties. The DC conductivities of the  $\text{MSn}_4\text{Se}_{10}^{2-}$  ( $M = \text{Fe}, \text{Mn}$ ) frameworks were ascribed primarily to ion transport and reported to be as

low as  $10^{-10}$  S/cm,<sup>28</sup> compared to the  $\sim 10^{-6}$  S/cm reported here for  $\text{FeGe}_4\text{S}_{10}^{2-}$ , which is dominated by electron transport. Such low electronic conductivity is surprising given the covalency of the Fe–S bonds, but it may be explained by low charge carrier densities afforded by the air-free synthetic conditions.

Finally, these results reveal mixed-conducting and magnetic ordering behavior previously unknown for open-framework chalcogenides. The ferromagnetic ordering of  $\text{TMA}_2\text{FeGe}_4\text{S}_{10}$  observed at  $\sim 2.75$  K provides the first validation of an earlier computational study on this family of material, which predicted ferromagnetism in the Fe variant but not the other analogues.<sup>62</sup> This study also predicted half-metallicity, which has yet to be reported. The absence of ferromagnetic ordering in Fe–Se likely reflects the increased distance between Fe sites and/or the Fe sites being predominantly  $\text{Fe}^{3+}$  centers. This may explain the absence of magnetic ordering in the previously studied  $\text{TMA}_2\text{FeSn}_4\text{Se}_{10}$ .<sup>33</sup> Although open-framework chalcogenides have been widely studied as ionic conductors, the EIS data in Figure 7c demonstrate hallmark evidence of mixed ion–electron conductivity. Given the ability of these materials to be prepared with other cations, such as Cs,<sup>34</sup> K,<sup>28</sup> and Li,<sup>36</sup> their propensity for cation exchange,<sup>24</sup> and the variable pore sizes and environments, coupled with the tunable electronic conductivity reported here, these results reveal that open-framework chalcogenides comprise an attractive new class of mixed conductors for studying energy storage and other electrochemical technologies.

## CONCLUSIONS

In conclusion, we report the preparation of two new open-framework chalcogenides,  $\text{TMA}_2\text{NiGe}_4\text{S}_{10}$  and  $\text{TMA}_2\text{CoGe}_4\text{Se}_{10}$ , and investigate the electronic, magnetic, and charge transport properties of these new members and previously reported isostructural analogues. Comparison of these materials through conductivity measurements and DFT methods shows that the identity of the metal ions and chalcogenides controls charge transport by dictating the composition and curvature of the valence and conduction bands and hence the charge carrier mobilities. The Fe-containing variants exhibit the highest conductivities, whereas all other variants display similar DC conductivity magnitudes. Impedance spectroscopy reveals that charge transport in the former involves mostly electrons, whereas the latter depends on both ions and electrons. This insight and the strong dependence on the amount of oxidized metal ion dopants suggest that charge transport in the frameworks proceeds by a band-type mechanism that improves with dilute concentrations of holes but which diminishes at high concentrations due to structural distortions that flatten band curvatures. Although open-framework chalcogenides are well established, these results provide some of the only insights into their tunable physical properties, proving that they remain a powerful platform for studying fundamental aspects of porous materials.

## METHODS

**Materials.** All commercial chemicals were used as received unless stated otherwise. Germanium powder (99.99%, Sigma-Aldrich), sublimed sulfur powder (99%, Strem), tetramethyl ammonium hydroxide pentahydrate (95%, Oakwood), selenium powder (99.7%, Acros Organics), iron(II) chloride tetrahydrate (98%, Alfa Aesar), iron(II) chloride (anhydrous, Strem), nickel(II) chloride hexahydrate (98%, Alfa Aesar), cobalt(II) acetate tetrahydrate (98%, Alfa Aesar),

zinc(II) acetate dihydrate (98%, Sigma-Aldrich), iron(III) chloride hexahydrate (97%, Strem), manganese(II) chloride tetrahydrate (ACS grade, Baker), zinc(II) nitrate hexahydrate (98%, Sigma-Aldrich), barium sulfate (97.5%, Baker), *N,N*-dimethyl-*p*-phenylenediamine (97%, Sigma-Aldrich), ferrocenium hexafluorophosphate (FcPF<sub>6</sub>, 97%, Sigma-Aldrich), naphthalene (99%, Sigma-Aldrich), hydrochloric acid (reagent grade, Sigma-Aldrich), hexanes (*n*-hexane, 45%, Oakwood Chemical), tetrahydrofuran (SPS grade, Oakwood Chemical), and ethanol (200 proof, Decon Labs). Solvothermal syntheses were conducted in autoclave PAAR bombs in a Yamato Convection oven unless stated otherwise.

**Synthetic Procedures: TMA<sub>4</sub>Ge<sub>4</sub>S<sub>10</sub>.** Following a procedure adapted from Yaghi et al.,<sup>24</sup> germanium powder (1 g, 13.76 mmol), sulfur powder (1.766 g, 6.88 mmol), and water (7.439 g, 412.8 mmol) were added to a Teflon Parr bomb. While slowly stirring this mixture with a glass rod, tetramethyl ammonium hydroxide pentahydrate (4.990 g, 27.53 mmol) was added and then the Parr bomb was sealed and placed in a fixed temperature oven at 150 °C for 15 h. The resulting yellow solution was vacuum-filtered to remove unreacted germanium, and then ~500 mL of acetone was added to induce precipitation of a white solid. The white powder was washed with acetone (20 mL × 3), hot toluene (20 mL × 3), and hexanes (20 mL × 3) and then dried overnight under dynamic vacuum to afford an off-white powder. The resulting product was stored under a positive N<sub>2</sub> atmosphere.

**TMA<sub>4</sub>Ge<sub>4</sub>Se<sub>10</sub>.** Following a procedure adapted from Homayoun Ahari et al.,<sup>37</sup> germanium powder (0.89 g, 12.2 mmol), selenium powder (2.43 g, 30.7 mmol), and water (4.4 g, 244 mmol) were added to a Teflon Parr bomb. While slowly stirring this mixture with a glass rod, tetramethyl ammonium hydroxide pentahydrate (2.28 g, 12.5 mmol) was added. The Parr bomb was sealed and then placed in a fixed temperature oven at 150 °C for 72 h. The resulting yellow solution was vacuum-filtered to remove unreacted germanium before ~500 mL of acetone was added to the solution, causing instant orange precipitation. The orange powder was subsequently washed with acetone (20 mL × 3), hot toluene (20 mL × 3), and hexanes (20 mL × 3) and then dried overnight under dynamic vacuum to afford a red-orange powder. The resulting product was stored under a positive N<sub>2</sub> atmosphere.

**TMA<sub>2</sub>MGe<sub>4</sub>S<sub>10</sub> Framework Syntheses.** All procedures were adapted from the original synthesis of TMA<sub>2</sub>MnGe<sub>4</sub>S<sub>10</sub> by Yaghi et al.<sup>24</sup>

**TMA<sub>2</sub>MnGe<sub>4</sub>S<sub>10</sub>.** Manganese(II) chloride tetrahydrate (0.0776 g, 0.392 mmol) and TMA<sub>4</sub>Ge<sub>4</sub>S<sub>10</sub> (0.178 g, 0.196 mmol) were dissolved in 4 mL of ethanol and 8 mL of DI water, respectively. To the TMA<sub>4</sub>Ge<sub>4</sub>S<sub>10</sub> solution, the manganese solution was added dropwise over the course of ~2 min. The resulting mixture was allowed to react at room temperature for ~12 h. The white solid was washed with DI water (15 mL × 3) and then dried in a fixed temperature oven at 150 °C for ~12 h. The resulting material was stored under ambient conditions.

**TMA<sub>2</sub>FeGe<sub>4</sub>S<sub>10</sub> (In-Air Synthesis).** Iron(II) chloride tetrahydrate (0.0779 g, 0.392 mmol) and TMA<sub>4</sub>Ge<sub>4</sub>S<sub>10</sub> (0.178 g, 0.196 mmol) were dissolved in 4 and 8 mL of DI water, respectively. The iron solution was added dropwise to the TMA<sub>4</sub>Ge<sub>4</sub>S<sub>10</sub> solution over the course of ~2 min. The resulting mixture was allowed to react at room temperature for ~12 h. The bright orange solid was washed with DI water (15 mL × 3) and then dried in a fixed temperature oven at 150 °C for ~12 h. The resulting material was stored under ambient conditions.

**TMA<sub>2</sub>FeGe<sub>4</sub>S<sub>10</sub> (Air-Free Synthesis).** Anhydrous iron(II) chloride (0.0497 g, 0.392 mmol) and TMA<sub>4</sub>Ge<sub>4</sub>S<sub>10</sub> (0.178 g, 0.196 mmol) were dissolved in 4 and 8 mL of N<sub>2</sub>-sparged DI water, respectively, under a positive nitrogen atmosphere. The iron solution was added dropwise to the TMA<sub>4</sub>Ge<sub>4</sub>S<sub>10</sub> solution over the course of ~2 min. The solution was allowed to react at room temperature for ~12 h. The bright orange solid was washed with sparged DI water (15 mL × 2), ethanol (15 mL × 2), and hexanes (15 mL × 2) sequentially. Then, the solid was dried with a stream of nitrogen and stored under a positive N<sub>2</sub> atmosphere.

**TMA<sub>2</sub>CoGe<sub>4</sub>S<sub>10</sub>.** Cobalt(II) acetate tetrahydrate (0.0976 g, 0.392 mmol) and TMA<sub>4</sub>Ge<sub>4</sub>S<sub>10</sub> (0.178 g, 0.196 mmol) were dissolved in 4 mL of ethanol and 8 mL of DI water, respectively. The cobalt solution was added dropwise to the TMA<sub>4</sub>Ge<sub>4</sub>S<sub>10</sub> solution over the course of ~2 min. The solution was left to react at room temperature for ~12 h. The teal solid was washed with DI water (15 mL × 3) and then dried in a fixed temperature oven at 150 °C for ~12 h. The resulting material was stored under ambient conditions.

**TMA<sub>2</sub>NiGe<sub>4</sub>S<sub>10</sub>.** Nickel(II) chloride hexahydrate (0.0932 g, 0.392 mmol) and TMA<sub>4</sub>Ge<sub>4</sub>S<sub>10</sub> (0.178 g, 0.196 mmol) were dissolved in 4 mL of ethanol and 8 mL of DI water, respectively. The nickel solution was added dropwise to the TMA<sub>4</sub>Ge<sub>4</sub>S<sub>10</sub> solution over the course of ~2 min. The solution was left to react at room temperature for ~12 h. The brown solid was washed with DI water (15 mL × 3) and then dried in a fixed temperature oven at 150 °C for ~12 h. The resulting material was stored under ambient conditions.

**TMA<sub>2</sub>ZnGe<sub>4</sub>S<sub>10</sub>.** Zinc(II) nitrate hexahydrate (0.1166 g, 0.392 mmol) and TMA<sub>4</sub>Ge<sub>4</sub>S<sub>10</sub> (0.178 g, 0.196 mmol) were dissolved in 4 and 8 mL of DI water, respectively. The zinc solution was added dropwise to the TMA<sub>4</sub>Ge<sub>4</sub>S<sub>10</sub> solution over the course of ~2 min. The resulting solution was left to react at room temperature for ~12 h. The white solid was washed with DI water (15 mL × 3) and then dried in a fixed temperature oven at 150 °C for ~12 h. The resulting material was stored under ambient conditions.

**TMA<sub>2</sub>MGe<sub>4</sub>Se<sub>10</sub> Framework Syntheses.** All procedures were adapted from a previous report by Ahari et al.<sup>37</sup>

**TMA<sub>2</sub>FeGe<sub>4</sub>Se<sub>10</sub> (In-Air Synthesis).** Iron(II) chloride tetrahydrate (0.0779 g, 0.392 mmol) and TMA<sub>4</sub>Ge<sub>4</sub>Se<sub>10</sub> (0.270 g, 0.196 mmol) were dissolved in 4 and 8 mL of DI water, respectively. The iron solution was added dropwise to the TMA<sub>4</sub>Ge<sub>4</sub>Se<sub>10</sub> solution over the course of ~2 min. The solution was left to react at room temperature for ~12 h. The resulting maroon solid was washed with DI water (15 mL × 3) and then dried in a fixed temperature oven at 150 °C for ~12 h. The resulting material was stored under ambient conditions.

**TMA<sub>2</sub>FeGe<sub>4</sub>Se<sub>10</sub> (Air-Free Synthesis).** Anhydrous iron(II) chloride (0.0497 g, 0.392 mmol) and TMA<sub>4</sub>Ge<sub>4</sub>Se<sub>10</sub> (0.270 g, 0.196 mmol) were dissolved in 4 and 8 mL of sparged DI water, respectively, under a positive nitrogen atmosphere. The iron solution was added dropwise to the TMA<sub>4</sub>Ge<sub>4</sub>Se<sub>10</sub> solution over the course of ~2 min. The solution was left to react at room temperature for ~12 h. The resulting maroon solid was washed with sparged DI water (15 mL × 2), ethanol (15 mL × 2), and hexanes (15 mL × 2) sequentially. Then, the solid was dried with a stream of nitrogen and stored under a positive nitrogen atmosphere.

**Characterization.** Sample purity and crystallinity were verified by powder X-ray diffraction (PXRD) with a Bruker D2 Phaser benchtop diffractometer. Diffuse reflectance UV–vis was performed on a Perkin Elmer Lambda-1050 UV/vis/NIR spectrophotometer with Harrick Scientific Praying Mantis Diffuse Reflection (DRP) accessory and PMT, InGaAs, and PbS 3-detector modules. All samples were diluted with ground barium sulfate. Reflectance UV–vis spectra were collected in the range of 200–2000 nm with a 2 nm resolution unless stated otherwise.

**Pressed Pellet Conductivity Measurements.** Pressed pellets were prepared by compressing powders in a modified KBr pellet press die set with a hydraulic press at 2000 psi for 30 min. The pellet press die set had tinned copper wires affixed to both sides with silver paint and epoxy. Electrical contact was made by pressing a pellet with the modified die set with the stainless steel circular ends acting as the two electrodes. Direct current (DC) conductivities were determined from the slopes of current–voltage (*I*–*V*) curves collected with a GAMRY Instruments Interface 5000E potentiostat, along with the electrode area (0.402 cm<sup>2</sup>) and pellet thickness, according to the equation below (where *C* is the slope of the *I*–*V* curve and *m* is the pellet thickness)

$$DC_{\sigma} = \frac{C \times m}{0.402}$$

Samples were voltammetrically swept at 2 mV/s between  $-0.2$  ( $-0.1$ ) and  $0.1$  V while compressed at 1500 psi. Temperature-dependent measurements were conducted in a similar fashion with samples kept at fixed temperatures in a Yamato Convection oven.

**Pressed Pellet EIS Measurements.** Using the same setup for pressed pellet measurements and preparation, AC measurements were run with a DC voltage of 0 V with an AC amplitude of 150 mV from 2 MHz to 0.1 Hz.

**$^{57}\text{Fe}$  Mössbauer Spectroscopy.** All samples were characterized by a SEE Co.  $^{57}\text{Fe}$  Mössbauer spectrometer equipped with a Janis SVT-400 cryostat. The samples were prepared under a nitrogen atmosphere by placing up to 30 mg of fine powder in a 14.5 mm Teflon cup with a Teflon plunger pressed into the cup to hold the sample. Data were collected until the signal-to-noise was deemed sufficient for meaningful analysis. This was dependent on the amount of sample loaded and the intensity of the source but was typically longer than 1 week. Samples were maintained under a nitrogen atmosphere for the duration of the experiment. Calibration of the instrument was performed using a standard iron sample provided by SEE Co. The data were analyzed using the Mössbauer spectral analysis software WMOSS4<sup>63</sup> written by Tom Kent and recently developed by Ion Prisecaru. The raw data were folded and calibrated using the iron standard supplied to us. The folded data were then fit to an appropriate model. We used two models to fit the data for this paper: the first is used for a pair of quadrupole doublets, and the second model is for a single quadrupole doublet. We used these models to refine the relevant parameters such as the shift of the quadrupole peak and the relative area of the peaks.

**SQUID Magnetic Susceptibility Measurements.** Direct current (DC) susceptibility measurements were performed with a Quantum Design MPMS-XL SQUID magnetometer. Samples were prepared under an inert atmosphere as finely ground microcrystalline powders sealed in polyethylene baggies. Dc susceptibility measurements were performed at fields of 1000, 5000, and 10000 Oe. Ac susceptibility measurements were performed at zero DC field with an AC field of 4 Oe. The data were corrected for the diamagnetic contributions of the sample holder and the sample itself through the use of Pascal's constants.<sup>64</sup> Magnetization curves ( $M$  vs.  $H$ ) were recorded at 100 K from 0 to 3 T to check for the presence of unwanted ferromagnetic impurities.

**XPS Measurements.** X-ray photoelectron spectroscopy was performed on a ThermoScientific ESCALAB 250 X-ray photoelectron spectrometer. A survey scan was used to determine elements present before high-resolution scans were done on elements of interest. The binding energy scale was shifted to the hydrocarbon peak given by the tetramethyl ammonium cations residing within the frameworks.

**Chemical Oxidation of  $\text{TMA}_2\text{MGe}_4\text{S}_{10}$  ( $M = \text{Mn, Co, and Ni}$ ).** Under an inert nitrogen atmosphere, 26 mg (0.78 mmol) of  $\text{FcPF}_6$  was dissolved in 4 mL of THF and left to stir for  $\sim 2$  h. Fifteen milligrams of each framework was added to the respective vials and 1 mL of the  $\text{FcPF}_6$  solution was added to each. The vials were left to stir overnight. The frameworks were then washed with THF (10 mL  $\times$  3) and then dried under dynamic vacuum at room temperature.

**Chemical Oxidation of  $\text{TMA}_2\text{FeGe}_4\text{S}_{10}$ .** The ferrocenium tetrafluoroborate stock solution was made by dissolving 0.3164 g of ferrocenium tetrafluoroborate in 10 mL of THF and left to stir overnight. Fe-S powder was suspended in 5 mL of THF and left to stir. To the stirring solution, 1 mL of the stock ferrocenium solution was added (1.5 equiv) to one vial and 275  $\mu\text{L}$  (0.5 equiv) to another vial. The reactions were left to react for 36 h. To wash them, the solids were centrifuged down under a positive  $\text{N}_2$  pressure. The solids were then washed with THF (30 mL  $\times$  2) and hexanes (30 mL  $\times$  1).

**Potential-Dependent Conductivity.** A 0.1 M  $\text{TBAPF}_6$  solution was prepared by dissolving 3.87 g of  $\text{TBAPF}_6$  in 100 mL of acetonitrile under a positive nitrogen pressure. A three-electrode electrochemical cell was constructed (see Schematic S1) by immersing a pressed pellet of  $\text{TMA}_2\text{FeGe}_4\text{S}_{10}$  into a sparged electrolyte solution (0.1 M  $\text{TBAPF}_6$  in acetonitrile). An insulated copper wire was appended to one side of the pellet by silver paint, with epoxy insulating the electrical contact to the pellet. A  $\text{Ag}/\text{AgNO}_3$

pseudo-reference was utilized as well as a carbon counter electrode. A standard three-contact experiment was set up using a GAMRY Instruments Interface 5000E potentiostat. EIS measurements were collected with 25 mV AC perturbations at different DC voltages ( $-0.3$ – $0.9$  V) relative to the open-circuit potential. The bulk resistance of the pellet was determined by the low-frequency near-intersection on the  $x$ -axis of the Nyquist plot.

**Ligand Field Analysis.** Transitions were assigned according to the literature precedent,<sup>65</sup> and ligand field parameters were determined using mathematical equations from Lever.<sup>66</sup>  $B'$  is defined as the reduction in the interelectronic repulsion parameter ( $B$ ) when in the framework compared to the  $B$  value for the free metal ion, as calculated by the equation below (where  $B$  is the experimental interelectronic repulsion parameter and  $B_f$  is the interelectronic repulsion parameter of the free metal ion)

$$B': \left( \frac{B - B_f}{B} \right) \times 100$$

**Le Bail Fits and Rietveld Refinements.** To confirm the purity of samples as well as index the new isostructural analogues ( $\text{TMA}_2\text{NiGe}_4\text{S}_{10}$  and  $\text{TMA}_2\text{CoGe}_4\text{Se}_{10}$ ), general structure analysis system (GSAS) was utilized for Le Bail fits and Rietveld refinements. The known crystal structures of  $\text{TMA}_2\text{MnGe}_4\text{S}_{10}$  and  $\text{TMA}_2\text{FeGe}_4\text{Se}_{10}$ <sup>24,34</sup> were used to index the other experimental powder patterns, and the refined unit cell parameters are summarized in Table S1. As a general note, the FWHM parameters  $U$ ,  $V$ ,  $W$ ,  $X$ , and  $Y$ , sample displacement, and unit cell lattice parameters  $a$  and  $c$  were refined in each Le Bail fit. The fits were determined to be feasible structural solutions to the given powder patterns.<sup>67</sup>

**Computational Methods.** Structural optimizations for all materials were performed with DFT, as implemented in the Vienna ab initio simulation package (VASP, version 5.4.4).<sup>68</sup> All structures were equilibrated using the unrestricted GGA-PBESol exchange–correlation functional<sup>69</sup> with the PAW plane-wave method.<sup>70</sup> Ionic relaxation was achieved when all forces were smaller than 0.005 eV/Å. The plane-wave cutoff was set at 500 eV, and the SCF convergence criterion was  $10^{-6}$  eV, resulting in an electronic convergence of 0.005 eV per atom. An automatic  $k$ -grid was used during the optimization with  $3 \times 3 \times 2$  sampling. Single-point calculations were performed with a  $3 \times 3 \times 2$   $k$ -grid to obtain initial wavefunctions before electronic property calculations.

Electronic band structures along with partial density of states (pDOS) for each optimized structure were constructed with the HSEsol06<sup>71</sup> (PBESol + 25% HF) level of theory and with similar convergence criteria as the above sampling along the high-symmetry  $k$ -path, as shown in each band structure. A Gaussian was applied to smear the DOS, using  $\sigma = 0.05$ . The Fermi levels were then drawn at the DOS edge, rather than peak center. By convention, the corresponding optical gap for each optimized structure was then obtained from the valence band maximum and the conduction band minimum. Band decomposed charge density calculation at the  $\Gamma$ -point was performed to visualize the mixed-valence bands for the  $[\text{Fe}^{\text{III}}\text{Ge}_4\text{S}_{10}\text{TMA}]$  material.

## ■ ASSOCIATED CONTENT

### SI Supporting Information

The Supporting Information is available free of charge at <https://pubs.acs.org/doi/10.1021/acs.chemmater.1c04285>.

Additional experimental synthetic procedures, data analysis methods, optical and XPS spectra, X-ray patterns, and magnetization data (PDF)

## ■ AUTHOR INFORMATION

### Corresponding Authors

Christopher H. Hendon – Department of Chemistry and Biochemistry, Materials Science Institute, University of

Oregon, Eugene, Oregon 97403, United States; [orcid.org/0000-0002-7132-768X](https://orcid.org/0000-0002-7132-768X); Email: [chendon@uoregon.edu](mailto:chendon@uoregon.edu)

**Carl K. Brozek** – Department of Chemistry and Biochemistry, Materials Science Institute, University of Oregon, Eugene, Oregon 97403, United States; [orcid.org/0000-0002-8014-7904](https://orcid.org/0000-0002-8014-7904); Email: [cbrozek@uoregon.edu](mailto:cbrozek@uoregon.edu)

## Authors

**Jacob McKenzie** – Department of Chemistry and Biochemistry, Materials Science Institute, University of Oregon, Eugene, Oregon 97403, United States

**Khoa N. Le** – Department of Chemistry and Biochemistry, Materials Science Institute, University of Oregon, Eugene, Oregon 97403, United States

**Dylan J. Bardgett** – Department of Chemistry and Biochemistry, Materials Science Institute, University of Oregon, Eugene, Oregon 97403, United States

**Kelsey A. Collins** – Department of Chemistry, Northwestern University, Evanston, Illinois 60208, United States

**Thomas Ericson** – Department of Chemistry and Biochemistry, Texas Tech University, Lubbock, Texas 79409, United States

**Michael K. Wojnar** – Department of Chemistry, Massachusetts Institute of Technology, Cambridge, Massachusetts 02139, United States

**Julie Chouinard** – Center for Advanced Materials Characterization in Oregon, University of Oregon, Eugene, Oregon 97403, United States

**Stephen Golledge** – Center for Advanced Materials Characterization in Oregon, University of Oregon, Eugene, Oregon 97403, United States

**Anthony F. Cozzolino** – Department of Chemistry and Biochemistry, Texas Tech University, Lubbock, Texas 79409, United States; [orcid.org/0000-0002-1100-0829](https://orcid.org/0000-0002-1100-0829)

**David C. Johnson** – Department of Chemistry and Biochemistry, Materials Science Institute, University of Oregon, Eugene, Oregon 97403, United States; [orcid.org/0000-0002-1118-0997](https://orcid.org/0000-0002-1118-0997)

Complete contact information is available at:

<https://pubs.acs.org/10.1021/acs.chemmater.1c04285>

## Notes

The authors declare no competing financial interest.

## ACKNOWLEDGMENTS

This material was based upon work supported by the National Science Foundation through the Division of Materials Research under grant no. DMR-1956403 and through the Department of Energy through the Office of Basic Energy Sciences under grant no. DE-SC0022147. C.H.H. acknowledges the Research Corporation for Science Advances (Cottrell Award). The authors also acknowledge the continued support from the Extreme Science and Engineering Discovery Environment (XSEDE), which is supported by the National Science Foundation (ACI-1548562). The authors thank Dr. D. Freedman for assistance with magnetic measurement collection and analysis.

## REFERENCES

- (1) Liu, L.; Corma, A. Confining Isolated Atoms and Clusters in Crystalline Porous Materials for Catalysis. *Nat. Rev. Mater.* **2021**, *6*, 244–263.
- (2) Li, Y.; Yu, J. Emerging Applications of Zeolites in Catalysis, Separation and Host–Guest Assembly. *Nat. Rev. Mater.* **2021**, 1156–1174.
- (3) Liu, Y.; Wu, X.; Li, Z.; Zhang, J.; Liu, S.-X.; Liu, S.; Gu, L.; Zheng, L. R.; Li, J.; Wang, D.; Li, Y. Fabricating Polyoxometalates-Stabilized Single-Atom Site Catalysts in Confined Space with Enhanced Activity for Alkynes Diboration. *Nat. Commun.* **2021**, *12*, No. 4205.
- (4) Zywitzki, D.; Jing, H.; Tüysüz, H.; Chan, C. K. High Surface Area, Amorphous Titania with Reactive  $\text{Ti}^{3+}$  through a Photo-Assisted Synthesis Method for Photocatalytic  $\text{H}_2$  Generation. *J. Mater. Chem. A* **2017**, *5*, 10957–10967.
- (5) Yang, D.; Gates, B. C. Catalysis by Metal Organic Frameworks: Perspective and Suggestions for Future Research. *ACS Catal.* **2019**, *9*, 1779–1798.
- (6) Sheberla, D.; Bachman, J. C.; Elias, J. S.; Sun, C.-J.; Shao-Horn, Y.; Dincă, M. Conductive MOF Electrodes for Stable Supercapacitors with High Areal Capacitance. *Nat. Mater.* **2017**, *16*, 220–224.
- (7) Cheng, Q.; Okamoto, Y.; Tamura, N.; Tsuji, M.; Maruyama, S.; Matsuo, Y. Graphene-Like-Graphite as Fast-Chargeable and High-Capacity Anode Materials for Lithium Ion Batteries. *Sci. Rep.* **2017**, *7*, No. 14782.
- (8) Bi, S.; Banda, H.; Chen, M.; Niu, L.; Chen, M.; Wu, T.; Wang, J.; Wang, R.; Feng, J.; Chen, T.; Dincă, M.; Kornyshev, A. A.; Feng, G. Molecular Understanding of Charge Storage and Charging Dynamics in Supercapacitors with MOF Electrodes and Ionic Liquid Electrolytes. *Nat. Mater.* **2020**, *19*, 552–558.
- (9) Sun, C.; Rajasekhara, S.; Goodenough, J. B.; Zhou, F. Monodisperse Porous  $\text{LiFePO}_4$  Microspheres for a High Power Li-Ion Battery Cathode. *J. Am. Chem. Soc.* **2011**, *133*, 2132–2135.
- (10) Lee, E. J.; Lee, L.; Abbas, M. A.; Bang, J. H. The Influence of Surface Area, Porous Structure, and Surface State on the Supercapacitor Performance of Titanium Oxynitride: Implications for a Nanostructuring Strategy. *Phys. Chem. Chem. Phys.* **2017**, *19*, 21140–21151.
- (11) Liu, Z.; Yuan, X.; Zhang, S.; Wang, J.; Huang, Q.; Yu, N.; Zhu, Y.; Fu, L.; Wang, F.; Chen, Y.; Wu, Y. Three-Dimensional Ordered Porous Electrode Materials for Electrochemical Energy Storage. *NPG Asia Mater.* **2019**, *11*, 1–21.
- (12) Tao, X.; Gao, Y.; Wang, S.; Wang, X.; Liu, Y.; Zhao, Y.; Fan, F.; Dupuis, M.; Li, R.; Li, C. Interfacial Charge Modulation: An Efficient Strategy for Boosting Spatial Charge Separation on Semiconductor Photocatalysts. *Adv. Energy Mater.* **2019**, *9*, No. 1803951.
- (13) Renault, C.; Nicole, L.; Sanchez, C.; Costentin, C.; Balland, V.; Limoges, B. Unraveling the Charge Transfer/Electron Transport in Mesoporous Semiconductive  $\text{TiO}_2$  Films by Voltabsorptometry. *Phys. Chem. Chem. Phys.* **2015**, *17*, 10592–10607.
- (14) Fabregat-Santiago, F.; Mora-Seró, I.; Garcia-Belmonte, G.; Bisquert, J. Cyclic Voltammetry Studies of Nanoporous Semiconductors. Capacitive and Reactive Properties of Nanocrystalline  $\text{TiO}_2$  Electrodes in Aqueous Electrolyte. *J. Phys. Chem. B* **2003**, *107*, 758–768.
- (15) Foo, C.; Li, Y.; Lebedev, K.; Chen, T.; Day, S.; Tang, C.; Tsang, S. C. E. Characterisation of Oxygen Defects and Nitrogen Impurities in  $\text{TiO}_2$  Photocatalysts Using Variable-Temperature X-Ray Powder Diffraction. *Nat. Commun.* **2021**, *12*, No. 661.
- (16) Sun, X.; Zhang, X.; Xie, Y. Surface Defects in Two-Dimensional Photocatalysts for Efficient Organic Synthesis. *Matter* **2020**, *2*, 842–861.
- (17) Wu, S.; Tan, X.; Lei, J.; Chen, H.; Wang, L.; Zhang, J. Gd-Doped and Pt-Loaded Porous  $\text{TiO}_2$ – $\text{SiO}_2$  for Photocatalytic Nonoxidative Coupling of Methane. *J. Am. Chem. Soc.* **2019**, *141*, 6592–6600.
- (18) Xiao, W.; Yang, S.; Zhang, P.; Li, P.; Wu, P.; Li, M.; Chen, N.; Jie, K.; Huang, C.; Zhang, N.; Dai, S. Facile Synthesis of Highly Porous Metal Oxides by Mechanochemical Nanocasting. *Chem. Mater.* **2018**, *30*, 2924–2929.
- (19) Moosavi, S. M.; Nandy, A.; Jablonka, K. M.; Ongari, D.; Janet, J. P.; Boyd, P. G.; Lee, Y.; Smit, B.; Kulik, H. J. Understanding the

Diversity of the Metal–Organic Framework Ecosystem. *Nat. Commun.* **2020**, *11*, No. 4068.

(20) Xie, L. S.; Skorupskii, G.; Dincă, M. Electrically Conductive Metal–Organic Frameworks. *Chem. Rev.* **2020**, *120*, 8536–8580.

(21) Sheberla, D.; Sun, L.; Blood-Forsythe, M. A.; Er, S.; Wade, C. R.; Brozek, C. K.; Aspuru-Guzik, A.; Dincă, M. High Electrical Conductivity in  $\text{Ni}_3(2,3,6,7,10,11\text{-Hexaiminotriphenylene})_2$ , a Semiconducting Metal–Organic Graphene Analogue. *J. Am. Chem. Soc.* **2014**, *136*, 8859–8862.

(22) Dong, R.; Han, P.; Arora, H.; Ballabio, M.; Karakus, M.; Zhang, Z.; Shekhar, C.; Adler, P.; Petkov, P. S.; Erbe, A.; Mannsfeld, S. C. B.; Felser, C.; Heine, T.; Bonn, M.; Feng, X.; Cánovas, E. High-Mobility Band-like Charge Transport in a Semiconducting Two-Dimensional Metal–Organic Framework. *Nat. Mater.* **2018**, *17*, 1027–1032.

(23) Gándara, F.; Uribe-Romo, F. J.; Britt, D. K.; Furukawa, H.; Lei, L.; Cheng, R.; Duan, X.; O’Keeffe, M.; Yaghi, O. M. Porous, Conductive Metal-Triazolates and Their Structural Elucidation by the Charge-Flipping Method. *Chem. - Eur. J.* **2012**, *18*, 10595–10601.

(24) Yaghi, O. M.; Sun, Z.; Richardson, D. A.; Groy, T. L. Directed Transformation of Molecules to Solids: Synthesis of a Microporous Sulfide from Molecular Germanium Sulfide Cages. *J. Am. Chem. Soc.* **1994**, *116*, 807–808.

(25) Rangan, K. K.; Billinge, S. J. L.; Petkov, V.; Heising, J.; Kanatzidis, M. G. Aqueous Mediated Synthesis of Mesostructured Manganese Germanium Sulfide with Hexagonal Order. *Chem. Mater.* **1999**, *11*, 2629–2632.

(26) Bag, S.; Kanatzidis, M. G. Chalcogenide Networks from Main-Group Metal Ions. Effect of Surface Polarizability on Selectivity in Gas Separation. *J. Am. Chem. Soc.* **2010**, *132*, 14951–14959.

(27) Bag, S.; Kanatzidis, M. G. Importance of Solution Equilibria in the Directed Assembly of Metal Chalcogenide Mesostructures. *J. Am. Chem. Soc.* **2008**, *130*, 8366–8376.

(28) Haddadpour, S.; Melullis, M.; Staesche, H.; Mariappan, C. R.; Roling, B.; Clérac, R.; Dehnen, S. Inorganic Frameworks from Selenidotetrelate Anions  $[\text{T}_2\text{Se}_6]^{4-}$  (T = Ge, Sn): Synthesis, Structures, and Ionic Conductivity of  $[\text{K}_2(\text{H}_2\text{O})_3][\text{MnGe}_4\text{Se}_{10}]$  and  $(\text{NMe}_4)_2[\text{MSn}_4\text{Se}_{10}]$  (M = Mn, Fe). *Inorg. Chem.* **2009**, *48*, 1689–1698.

(29) Rangan, K. K.; Trikalitis, P. N.; Kanatzidis, M. G. Light-Emitting Meso-Structured Sulfides with Hexagonal Symmetry: Supramolecular Assembly of  $[\text{Ge}_4\text{S}_{10}]^{4+}$  Clusters with Trivalent Metal Ions and Cetylpyridinium Surfactant. *J. Am. Chem. Soc.* **2000**, *122*, 10230–10231.

(30) MacLachlan, M. J.; Coombs, N.; Bedard, R. L.; White, S.; Thompson, L. K.; Ozin, G. A. Mesostructured Metal Germanium Sulfides. *J. Am. Chem. Soc.* **1999**, *121*, 12005–12017.

(31) Zhang, J.; Bu, X.; Feng, P.; Wu, T. Metal Chalcogenide Supertetrahedral Clusters: Synthetic Control over Assembly, Dispersibility, and Their Functional Applications. *Acc. Chem. Res.* **2020**, *53*, 2261–2272.

(32) MacLachlan, M. J.; Coombs, N.; Ozin, G. A. Non-Aqueous Supramolecular Assembly of Mesostructured Metal Germanium Sulphides from  $(\text{Ge}_4\text{S}_{10})^{4-}$  Clusters. *Nature* **1999**, *397*, 681–684.

(33) Tsamourtzi, K.; Song, J.-H.; Bakas, T.; Freeman, A. J.; Trikalitis, P. N.; Kanatzidis, M. G. Straightforward Route to the Adamantane Clusters  $[\text{Sn}_4\text{Q}_{10}]^{4-}$  (Q = S, Se, Te) and Use in the Assembly of Open-Framework Chalcogenides  $(\text{Me}_4\text{N})_2\text{M}[\text{Sn}_4\text{Se}_{10}]$  (M =  $\text{Mn}^{\text{II}}$ ,  $\text{Fe}^{\text{II}}$ ,  $\text{Co}^{\text{II}}$ ,  $\text{Zn}^{\text{II}}$ ) Including the First Telluride Member  $(\text{Me}_4\text{N})_2\text{Mn}[\text{Ge}_4\text{Te}_{10}]$ . *Inorg. Chem.* **2008**, *47*, 11920–11929.

(34) Bowes, C. L.; Lough, A. J.; Malek, A.; Ozin, G. A.; Petrov, S.; Young, D. Thermally Stable Self-Assembling Open-Frameworks: Isostructural  $\text{Cs}^+$  and  $(\text{CH}_3)_4\text{N}^+$  Iron Germanium Sulfides. *Chem. Ber.* **1996**, *129*, 283–287.

(35) Trikalitis, P. N.; Rangan, K. K.; Bakas, T.; Kanatzidis, M. G. Varied Pore Organization in Mesostructured Semiconductors Based on the  $[\text{SnSe}_4]^{4-}$  Anion. *Nature* **2001**, *410*, 671–675.

(36) Duchardt, M.; Haddadpour, S.; Kaib, T.; Bron, P.; Roling, B.; Dehnen, S. Different Chemical Environments of  $[\text{Ge}_4\text{Se}_{10}]^{4-}$  in the

$\text{Li}^+$  Compounds  $[\text{Li}_4(\text{H}_2\text{O})_{16}][\text{Ge}_4\text{Se}_{10}] \cdot 4.33\text{H}_2\text{O}$ ,  $[\{\text{Li}_4(\text{Thf})_{12}\}-\text{Ge}_4\text{Se}_{10}]$ , and  $[\text{Li}_2(\text{H}_2\text{O})_8][\text{MnGe}_4\text{Se}_{10}]$ , and Ionic Conductivity of Underlying  $[\text{Li}_4\text{Ge}_4\text{Se}_{10}]$ . *Inorg. Chem.* **2021**, *60*, 5224–5231.

(37) Ahari, H.; Garcia, A.; Kirkby, S.; Ozin, G. A.; Young, D.; Lough, A. J. Self-Assembling Iron and Manganese Metal–Germanium–Selenide Frameworks:  $[\text{NMe}_4]_2\text{MGe}_4\text{Se}_{10}$ , Where M = Fe or Mn. *J. Chem. Soc., Dalton Trans.* **1998**, 2023–2028.

(38) Mas-Ballesté, R.; Gómez-Navarro, C.; Gómez-Herrero, J.; Zamora, F. 2D Materials: To Graphene and Beyond. *Nanoscale* **2011**, *3*, 20–30.

(39) Li, Y.; Jiang, X.; Fu, Z.; Huang, Q.; Wang, G.-E.; Deng, W.-H.; Wang, C.; Li, Z.; Yin, W.; Chen, B.; Xu, G. Coordination Assembly of 2D Ordered Organic Metal Chalcogenides with Widely Tunable Electronic Band Gaps. *Nat. Commun.* **2020**, *11*, No. 261.

(40) Gütllich, P.; Bill, E.; Trautwein, A. X. Hyperfine Interactions. In *Mössbauer Spectroscopy and Transition Metal Chemistry: Fundamentals and Applications*; Springer:Berlin, Heidelberg, 2011; pp 73–135.

(41) Levesanos, N.; Liyanage, W. P. R.; Ferentinos, E.; Raptopoulos, G.; Paraskevopoulou, P.; Sanakis, Y.; Choudhury, A.; Stavropoulos, P.; Nath, M.; Kyritsis, P. Investigating the Structural, Spectroscopic, and Electrochemical Properties of  $[\text{Fe}\{\text{E}(\text{PiPr}_2)_2\text{N}\}_2]$  (E = S, Se) and the Formation of Iron Selenides by Chemical Vapor Deposition. *Eur. J. Inorg. Chem.* **2016**, 2016, 5332–5339.

(42) Weakliem, H. A. Optical Spectra of  $\text{Ni}^{2+}$ ,  $\text{Co}^{2+}$ , and  $\text{Cu}^{2+}$  in Tetrahedral Sites in Crystals. *J. Chem. Phys.* **1962**, *36*, 2117–2140.

(43) Dalal, M. A. *Textbook of Inorganic Chemistry*; Dalal Institute, 2017; Vol. 1.

(44) Jamnik, J.; Maier, J. Treatment of the Impedance of Mixed Conductors Equivalent Circuit Model and Explicit Approximate Solutions. *J. Electrochem. Soc.* **1999**, *146*, 4183.

(45) Deaton, J. C.; Gebhard, M. S.; Koch, S. A.; Millar, M.; Solomon, E. I. Ligand Field Transitions and the Origin of Zero Field Splitting in  $[\text{PPh}_4][\text{FeCl}_4]$  and  $[\text{NET}_4][\text{Fe}(\text{SR})_4]$  (R = 2,3,5,6-Me<sub>4</sub>C<sub>6</sub>H): A Model for the High-Spin Fe(III) Site in Rubredoxin. *J. Am. Chem. Soc.* **1988**, *110*, 6241–6243.

(46) Syarifati, A.; Kumar, S.; Zahid, A.; Yumin, A. A. E.; Ye, J.; Rudolf, P. Photoemission Spectroscopy Study of Structural Defects in Molybdenum Disulfide ( $\text{MoS}_2$ ) Grown by Chemical Vapor Deposition (CVD). *Chem. Commun.* **2019**, *55*, 10384–10387.

(47) Mekar, H.; Yoshigoe, A.; Nakamura, M.; Doura, T.; Tamanoi, F. Biodegradability of Disulfide-Organosilica Nanoparticles Evaluated by Soft X-Ray Photoelectron Spectroscopy: Cancer Therapy Implications. *ACS Appl. Nano Mater.* **2019**, *2*, 479–488.

(48) Shuai, Z.; Li, W.; Ren, J.; Jiang, Y.; Geng, H. Applying Marcus Theory to Describe the Carrier Transports in Organic Semiconductors: Limitations and Beyond. *J. Chem. Phys.* **2020**, *153*, No. 080902.

(49) Lin, S.; Usov, P. M.; Morris, A. J. The Role of Redox Hopping in Metal–Organic Framework Electrocatalysis. *Chem. Commun.* **2018**, *54*, 6965–6974.

(50) Wilbourn, K.; Murray, R. W. The d.c. Redox versus Electronic Conductivity of the Ladder Polymer Poly-(Benzimidazobenzophenanthroline). *J. Phys. Chem. A* **1988**, *92*, 3642–3648.

(51) Feldman, B. J.; Burgmayer, P.; Murray, R. W. The Potential Dependence of Electrical Conductivity and Chemical Charge Storage of Poly(Pyrrrole) Films on Electrodes. *J. Am. Chem. Soc.* **1985**, *107*, 872–878.

(52) Sun, L.; Hendon, C. H.; Park, S. S.; Tulchinsky, Y.; Wan, R.; Wang, F.; Walsh, A.; Dincă, M. Is Iron Unique in Promoting Electrical Conductivity in MOFs? *Chem. Sci.* **2017**, *8*, 4450–4457.

(53) Sun, L.; Miyakai, T.; Seki, S.; Dincă, M.  $\text{Mn}_2(2,5\text{-Disulfhydrylbenzene-1,4-Dicarboxylate})$ : A Microporous Metal–Organic Framework with Infinite  $(-\text{Mn}-\text{S}-)_\infty$  Chains and High Intrinsic Charge Mobility. *J. Am. Chem. Soc.* **2013**, *135*, 8185–8188.

(54) Xie, L. S.; Sun, L.; Wan, R.; Park, S. S.; DeGayner, J. A.; Hendon, C. H.; Dincă, M. Tunable Mixed-Valence Doping toward Record Electrical Conductivity in a Three-Dimensional Metal–Organic Framework. *J. Am. Chem. Soc.* **2018**, *140*, 7411–7414.

(55) Sun, L.; Hendon, C. H.; Minier, M. A.; Walsh, A.; Dincă, M. Million-Fold Electrical Conductivity Enhancement in Fe<sub>2</sub>(DEBDC) versus Mn<sub>2</sub>(DEBDC) (E = S, O). *J. Am. Chem. Soc.* **2015**, *137*, 6164–6167.

(56) Park, J. G.; Aubrey, M. L.; Oktawiec, J.; Chakarawet, K.; Darago, L. E.; Grandjean, F.; Long, G. J.; Long, J. R. Charge Delocalization and Bulk Electronic Conductivity in the Mixed-Valence Metal–Organic Framework Fe(1,2,3-Triazolate)<sub>2</sub>(BF<sub>4</sub>)<sub>x</sub>. *J. Am. Chem. Soc.* **2018**, *140*, 8526–8534.

(57) DeGayner, J. A.; Jeon, I.-R.; Sun, L.; Dincă, M.; Harris, T. D. 2D Conductive Iron-Quinoid Magnets Ordering up to T<sub>c</sub> = 105 K via Heterogenous Redox Chemistry. *J. Am. Chem. Soc.* **2017**, *139*, 4175–4184.

(58) Huang, X.; Zhang, S.; Liu, L.; Yu, L.; Chen, G.; Xu, W.; Zhu, D. Superconductivity in a Copper(II)-Based Coordination Polymer with Perfect Kagome Structure. *Angew. Chem., Int. Ed.* **2018**, *57*, 146–150.

(59) Clough, A. J.; Orchanian, N. M.; Skelton, J. M.; Neer, A. J.; Howard, S. A.; Downes, C. A.; Piper, L. F. J.; Walsh, A.; Melot, B. C.; Marinescu, S. C. Room Temperature Metallic Conductivity in a Metal–Organic Framework Induced by Oxidation. *J. Am. Chem. Soc.* **2019**, *141*, 16323–16330.

(60) Clough, A. J.; Skelton, J. M.; Downes, C. A.; de la Rosa, A. A.; Yoo, J. W.; Walsh, A.; Melot, B. C.; Marinescu, S. C. Metallic Conductivity in a Two-Dimensional Cobalt Dithiolene Metal–Organic Framework. *J. Am. Chem. Soc.* **2017**, *139*, 10863–10867.

(61) Chen, L.; San, K. A.; Turo, M. J.; Gembicky, M.; Fereidouni, S.; Kalaj, M.; Schimpf, A. M. Tunable Metal Oxide Frameworks via Coordination Assembly of Preyssler-Type Molecular Clusters. *J. Am. Chem. Soc.* **2019**, *141*, 20261–20268.

(62) Wang, J.; Zhao, L.; Gong, K. First-Principle Study of the Half-Metallic Ferromagnetic Compound [(CH<sub>3</sub>)<sub>4</sub>N]<sub>2</sub>FeGe<sub>4</sub>S<sub>10</sub>. *J. Magn. Mater.* **2008**, *320*, 1696–1699.

(63) Prisecaru, I. WMOSS4 Mössbauer Spectral Analysis Software. <http://www.wmoss.org/> (Nov 12, 2021).

(64) Bain, G. A.; Berry, J. F. Diamagnetic Corrections and Pascal's Constants. *J. Chem. Educ.* **2008**, *85*, 532.

(65) BN, F.; Hitchman, M. The Electronic Spectra of Complexes. In *Ligand Field Theory and Its Applications*; Wiley, 1999; pp 211–213.

(66) Lever, A. B. P. Electronic spectra of some transition metal complexes: Derivation of Dq and B. *J. Chem. Educ.* **1968**, No. 711.

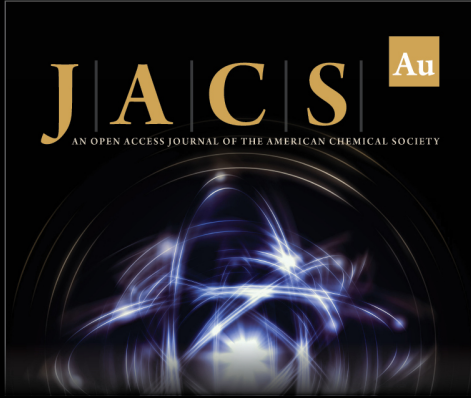
(67) Toby, B. H. R Factors in Rietveld Analysis: How Good Is Good Enough? *Powder Diffr.* **2006**, *21*, 67–70.

(68) Kresse, G.; Furthmüller, J. Efficiency of Ab-Initio Total Energy Calculations for Metals and Semiconductors Using a Plane-Wave Basis Set. *Comput. Mater. Sci.* **1996**, *6*, 15–50.

(69) Perdew, J. P.; Burke, K.; Ernzerhof, M. Generalized Gradient Approximation Made Simple. *Phys. Rev. Lett.* **1996**, *77*, 3865–3868.


(70) Blöchl, P. E. Projector Augmented-Wave Method. *Phys. Rev. B* **1994**, *50*, 17953–17979.


(71) Krukau, A. V.; Vydrov, O. A.; Izmaylov, A. F.; Scuseria, G. E. Influence of the Exchange Screening Parameter on the Performance of Screened Hybrid Functionals. *J. Chem. Phys.* **2006**, *125*, No. 224106.



**JACS** Au  
AN OPEN ACCESS JOURNAL OF THE AMERICAN CHEMICAL SOCIETY

Editor-in-Chief  
**Prof. Christopher W. Jones**  
Georgia Institute of Technology, USA

**Open for Submissions** 

pubs.acs.org/jacsau  ACS Publications  
Most Trusted. Most Cited. Most Read.